

Creative Commons Attribution 4.0 International (CC BY 4.0)

<https://creativecommons.org/licenses/by/4.0/>

Access to this work was provided by the University of Maryland, Baltimore County (UMBC) ScholarWorks@UMBC digital repository on the Maryland Shared Open Access (MD-SOAR) platform.

Please provide feedback

Please support the ScholarWorks@UMBC repository by emailing scholarworks-group@umbc.edu and telling us what having access to this work means to you and why it's important to you. Thank you.



Investigating the Superorbital Modulations in 4U 1909 + 07, IGR J16418-4532, and IGR J16479-4514 with Swift XRT, BAT, and NuSTAR Observations

Nazma Islam^{1,2} , Robin H. D. Corbet^{2,3,4} , Joel B. Coley^{5,6} , Katja Pottschmidt^{3,6} , and Felix Fuerst⁷

¹ Center for Space Science and Technology, University of Maryland, Baltimore County, 1000 Hilltop Circle, Baltimore, MD 21250, USA; nislam@umbc.edu

² X-ray Astrophysics Laboratory, NASA Goddard Space Flight Center, Greenbelt, MD 20771, USA

³ CRESST and CSST, University of Maryland, Baltimore County, 1000 Hilltop Circle, Baltimore, MD 21250, USA

⁴ Maryland Institute College of Art, 1300 W Mt Royal Avenue, Baltimore, MD 21217, USA

⁵ CRESST/Department of Physics and Astronomy, Howard University, Washington DC 20059, USA

⁶ Code 661 Astroparticle Physics Laboratory, NASA Goddard Space Flight Center, Greenbelt, MD 20771, USA

⁷ Quasar Science Resources S.L for European Space Agency (ESA), European Space Astronomy Centre (ESAC), Camino Bajo del Castillo s/n, E-28692 Villanueva de la Cañada, Madrid, Spain

Received 2022 October 28; revised 2023 February 10; accepted 2023 February 13; published 2023 May 4

Abstract

A puzzling variety of superorbital modulations has been discovered in several supergiant high mass X-ray binaries (sgHMXBs). To investigate the mechanisms driving these superorbital modulations, we have analyzed long-term Neil Gehrels Swift Observatory (Swift) Burst Alert Telescope (BAT) observations of three sgHMXBs: 4U 1909 + 07, IGR J16418–4532, and IGR J16479–4514, and constructed their dynamic power spectra and superorbital intensity profiles. These Swift BAT observations are complemented by pointed Swift X-ray Telescope (XRT) and Nuclear Spectroscopic Telescope Array (NuSTAR) observations performed near the predicted maximum and minimum phase of a single superorbital cycle for each of these sources. The BAT dynamic power spectra show changes in the strength of the superorbital modulation on timescales of years, with either the peak at the fundamental frequency and/or the second harmonic present at different times for all three sources. The pointed Swift XRT and NuSTAR observations show no significant differences between the pulse profiles and spectral parameters at the superorbital maximum and minimum phase. This is likely due to the fact the superorbital modulation had weakened significantly during the times when the NuSTAR observations were carried out for all three sources. The results from the Swift XRT, BAT, and NuSTAR analysis indicate the possible presence of multiple corotating interaction regions (CIRs) in the stellar winds of the supergiant stars, although a structured stellar wind from the supergiant star due to tidal oscillations cannot be ruled out.

Unified Astronomy Thesaurus concepts: High mass x-ray binary stars (733); Astronomy data analysis (1858); Stellar winds (1636)

1. Introduction

In addition to pulsations and orbital periods, a third type of periodicity is seen in many neutron star X-ray binaries. While the first two periodicities are attributed to the spin period of the neutron star (NS) and the binary orbit of the system, the causes of the third type of periodicity, which is longer than the orbital period and therefore called superorbital modulation, are still not fully understood. For systems where the accretion occurs by a Roche-lobe overflow via an accretion disk onto the NS such as Her X–1 (Leahy 2002; Staubert et al. 2009; Brumback et al. 2021), SMC X–1 (Wojdowski et al. 1998; Clarkson et al. 2003; Brumback et al. 2020), or LMC X–4 (Lang et al. 1981; Brumback et al. 2021), the superorbital modulation is attributed to the precession of the accretion disks, powered by the irradiation of the accretion disks by the NS (Ogilvie & Dubus 2001) or due to a change in the torque from an accretion disk (Hu et al. 2019). For high mass X-ray binaries (HMXBs) consisting of a Be star as a companion (Be-HMXBs), superorbital variability may be linked to the formation and dissipation of a circumstellar decretion disk around these systems (Rajoelimanana et al. 2011). Superorbital variability

has also been discovered in ultraluminous X-ray sources (ULXs), e.g., in M82 X–2 (~ 60 days; Brightman et al. 2019) and NGC 5907 ULX–1 (~ 78 days; Walton et al. 2016), where a strong correlation is found between their orbital and superorbital periods (Townsend & Charles 2020).

Supergiant high mass X-ray binaries (sgHMXBs) are X-ray binaries with mostly an NS as the compact object and an early-type O or B supergiant star as an optical companion. Supergiant fast X-ray transients (SFXTs) are a subclass of sgHMXBs that is characterized by a rapid flaring behavior during which the X-ray intensity increases a factor of $\sim 10^{3-4}$ or more. The accretion in sgHMXBs is mostly driven by strong stellar winds that are stochastic in nature and provide a less regularly structured environment compared to an accretion disk. However, superorbital modulations have been discovered in six sources at about three to four times their orbital period: 2S 0114 + 650 (Farrell et al. 2006), IGR J16493–4348, IGR J16418–4532, IGR J16479–4514, 4U 1909 + 07 (Drave et al. 2013a; Corbet & Krimm 2013), and 4U 1538–522 (Corbet et al. 2021). Since these systems do not have a decretion disk like Be-HMXBs and may or may not have a transient accretion disk, the mechanisms driving these superorbital modulations are still unknown.

Previous observations of 2S 0114 + 650 and IGR J16493–4348 as a function of their superorbital cycles showed a hardening in the spectral shape, which is indicative of a change in the mass transfer rate driving these superorbital



Original content from this work may be used under the terms of the [Creative Commons Attribution 4.0 licence](https://creativecommons.org/licenses/by/4.0/). Any further distribution of this work must maintain attribution to the author(s) and the title of the work, journal citation and DOI.

modulations (Farrell et al. 2008; Coley et al. 2019). A possible mechanism driving these changes in the mass transfer rate could be tidal oscillations induced in nonsynchronously rotating stars (Koenigsberger et al. 2006). Bozzo et al. (2017) proposed corotating interaction regions (CIRs) in the winds of these OB supergiant stars, which are characterized by spiral-shaped higher-density and velocity structures in the winds of the OB supergiant stars, extending up to tens of stellar radii. The beat frequency between a CIR and the NS orbit would cause this variation in X-ray intensities on superorbital timescales in sgHMXBs. Other models invoked to explain these intensity variations on superorbital timescales are NS precession models (Postnov et al. 2013), and the presence of a third star in a hierarchical system (Chou & Grindlay 2001), although they are unlikely to account for the superorbital modulations seen in HMXBs (Coley et al. 2019).

Superorbital modulations have been detected in 4U 1909 + 07, IGR J16418–4532, and IGR J16479–4514 using long-term Swift BAT light curves in 15–50 keV energy band (Corbet & Krimm 2013). The superorbital period estimated for 4U 1909 + 07, IGR J16418–4532, and IGR J16479–4514 is ~ 15.18 days, ~ 14.73 days, and ~ 11.88 days, respectively. In this paper, we analyze the long-term light curves of Swift BAT and pointed NuSTAR and Swift XRT observations of the above three sgHMXBs that were carried out at their predicted superorbital maximum and minimum phases from the ephemerides given in Corbet & Krimm (2013). The results from this analysis are used to investigate the possible mechanism driving these superorbital modulations.

1.1. Sample of Supergiant HMXBs Showing Superorbital Modulations

The source 4U 1909 + 07 is an accreting pulsar with a spin period of ~ 605 s and an orbital period of ~ 4.4 days (Levine et al. 2004). The optical companion is an early B-type (B0–B3) star, probably in its supergiant phase, and the distance to the system is estimated to be 4.85 ± 0.5 kpc (Martínez-Núñez et al. 2015). The system does not show an X-ray eclipse, but the X-ray flux is strongly modulated on its 4.4 days orbital period. A previous Chandra observation suggested a Compton shoulder on the Fe K α line, which indicates that the system is embedded in a Compton-thick environment (Torrejón et al. 2010). The spectrum of 4U 1909 + 07 from the Rossi X-ray Timing Explorer (RXTE) Proportional Counter Array (PCA), Suzaku, and International Gamma-Ray Astrophysics Laboratory (INTEGRAL) Soft Gamma-Ray Imager (ISGRI) observations revealed a high neutral hydrogen column density $N_H \sim 10^{23} \text{ cm}^{-2}$ and a power-law spectrum with a photon index of ~ 1 with a high-energy cutoff of ~ 20 keV, typical of an HMXB pulsar (Fürst et al. 2011, 2012).

IGR J16418–4532 is a candidate intermediate SFXT characterized by short X-ray flares (on timescales of an hour), reaching a dynamic X-ray flux range of $\sim 10^2$ (Sguera et al. 2006; Ducci et al. 2010). Bright X-ray flares have been observed from this system, reaching an X-ray luminosity of $10^{37} \text{ erg s}^{-1}$ (Romano et al. 2012b, 2012a; Krimm et al. 2013; Romano et al. 2015). From Swift XRT observations of this source, Romano et al. (2012b) found evidence of an inhomogeneous clumpy wind in the system, which could give rise to short X-ray flares seen in the light curve. It is an eclipsing X-ray binary with an orbital period of ~ 3.73 days (Corbet et al. 2006) and a spin period of ~ 1210 s

(Sidoli et al. 2012). The minimum distance to this binary system is estimated to be 13 kpc for a companion of the spectral type BN0.5Ia (Coleiro et al. 2013); however, from an eclipse timing analysis, Coley et al. (2015) found the spectral type of the optical companion star to be O8.5I or earlier. The X-ray spectrum of IGR J16418–4532 is highly absorbed with $N_H \sim 10^{23} \text{ cm}^{-2}$ and a power-law spectrum with a photon index of ~ 1 (Sidoli et al. 2012; Drave et al. 2013b). Using a 40 ks XMM-Newton observation, Sidoli et al. (2012) proposed that the observed X-ray variability and the quasiperiodic flaring activity are indicative of an NS accreting in a Transitional Roche-lobe overflow regime, that is, between pure wind accretion and Roche-lobe overflow.

IGR J16479–4514 is an eclipsing SFXT with an orbital period of 3.32 days (Jain et al. 2009). The nature of the compact object is unknown because no pulsations have been detected in the system. However, its spectrum is similar to that of accreting HMXB pulsars, suggesting an NS as the putative compact object. The optical companion is likely to be an O7 star, and this suggests a distance of 4.5 kpc to the binary system (Chaty et al. 2008; Coley et al. 2015). In addition to short low-luminosity X-ray flares lasting a few thousand seconds, orbital phase-locked X-ray flares are present in the light curve, with an occasional bright X-ray flare lasting few hours and reaching an X-ray flux of $10^{-9} \text{ erg cm}^{-2} \text{ s}^{-1}$ (Romano et al. 2008; Sguera et al. 2008; Sidoli et al. 2013; Sguera et al. 2020). These flares indicate large-scale structures in the stellar wind of the supergiant star (Bozzo et al. 2009; Sguera et al. 2020).

2. Data and Analysis

2.1. Long-term Observations with Swift BAT

The Swift BAT is a hard X-ray telescope that uses a coded mask and operates in the 14–195 keV energy band (Barthelmy et al. 2005). We used light curves from the BAT Transient Monitor⁸ (Krimm et al. 2013) in the 15–50 keV energy band from MJD 53,416 to MJD 59,515. The light curves were further screened to exclude bad quality points and to only use the data for which the data-quality flag “DATA_FLAG” was set to 0. A small number of data points with very low fluxes and unrealistically small uncertainties were also removed from the light curves (Corbet & Krimm 2013). The Swift BAT light curves of 4U 1909 + 07, IGR J16418–4532, and IGR J16479–4514 were used to construct the power spectra from MJD 53,415 to MJD 59,515 (16.7 yr, compared to ~ 8 yr of Swift BAT light curve used in Corbet & Krimm 2013). The power spectrum was calculated using the semi-weighting technique, in which the error bar on each data point and the excess variability in the light curve was taken into account (Corbet et al. 2007; Corbet & Krimm 2013). The significance of the peak at the superorbital period was estimated using the false-alarm probability (FAP; Scargle 1982). The uncertainty in the superorbital period measurement was obtained using the expression given in Horne & Baliunas (1986). The white-noise 99.99% significance level was calculated by fitting the continuum power levels in a narrow frequency range around the peak of interest. To investigate the contribution of the red noise to the power spectrum, we fit the logarithm of the power as a function of the logarithm of the frequency with a quadratic function (Vaughan 2005; Corbet et al. 2008). We found that the

⁸ <https://swift.gsfc.nasa.gov/results/transients/>

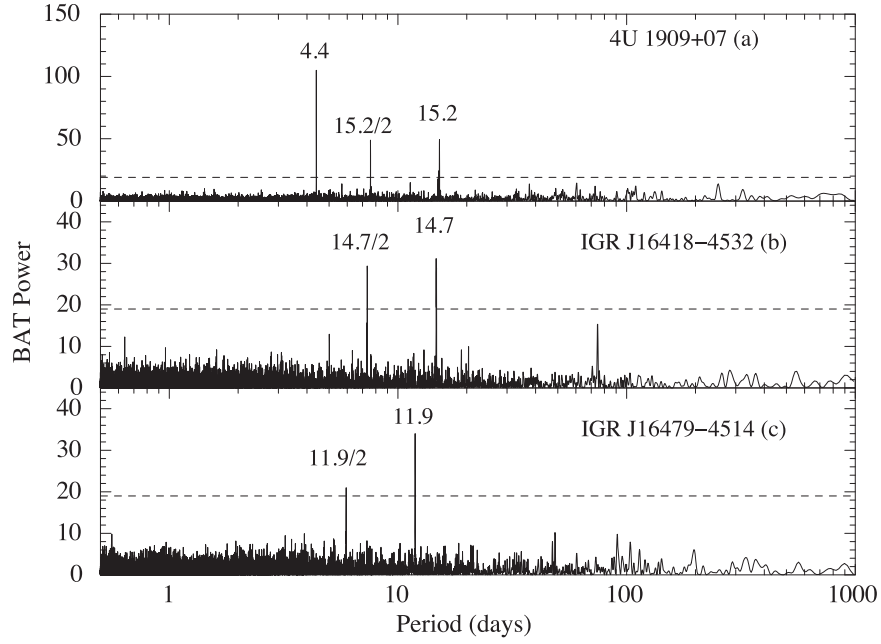


Figure 1. Power spectra from 16.7 yr of Swift BAT light curves of (a) 4U 1909 + 07, (b) IGR J16418–4532, and (c) IGR J16479–4514 in the energy band of 15–50 keV. The data points around the X-ray eclipse were removed from the light curves of IGR J16418–4532 and IGR J16479–4514 for the computation of the power spectra. The dashed lines indicate white-noise 99.99% significance levels. The power spectrum of 4U 1909 + 07 (a) exhibits prominent peaks at the orbital period of ~ 4.4 days, superorbital period of ~ 15.2 days, and the second harmonic of the superorbital period. The power spectrum of IGR J16418–4532 (b) exhibits prominent peaks at the superorbital period of ~ 14.7 days and the second harmonic. The power spectrum of IGR J16479–4514 (c) exhibits prominent peaks at the superorbital period of ~ 11.9 days and the second harmonic.

Table 1
Sample of sgHMXBs with Their Orbital and Superorbital Periods, and Their Orbital and Superorbital Ephemerides

Name	P_{orb}	T_{mid}	P_{super}^d	T_0^d	Spectral Type
4U 1909 + 07	4.4 ^a	...	15.196 ± 0.004	59502.1 ± 0.1	B0-B3 ^c
IGR J16418–4532	3.73880 ^b	55087.714 ^b	14.702 ± 0.004	59506.9 ± 0.1	O8.5I ^b
IGR J16479–4514	3.31961 ^b	55081.571 ^b	11.894 ± 0.006	59507.7 ± 0.1	O7 ^b

Notes.

^a –Levine et al. (2004).

^b –Coley et al. (2015).

^c –Martínez-Núñez et al. (2015).

^d This work; P_{orb} is the orbital period in days; P_{super} is the superorbital period in days; T_{mid} is the mid-eclipse time; T_0 is the time of the maximum flux of the average superorbital intensity profile.

continuum is flat, and therefore, the contribution of the red noise to the power spectrum of these sources is negligible in the superorbital period range of ~ 10 days.

The power spectrum of 4U 1909 + 07 plotted in panel (a) of Figure 1 exhibits prominent peaks at the orbital period of ~ 4.4 days, superorbital period of ~ 15.2 days, and the second harmonic of the superorbital period at ~ 7.6 days. The peaks at the superorbital period and the second harmonic are of equal strengths, with FAPs of $\sim 10^{-7}$. For IGR J16418–4532 and IGR J16479–4514, which have X-ray eclipses in their light curves, the power spectra were constructed after removing the data points lying inside the X-ray eclipse to mitigate the effects of the orbital modulation. We use the ephemerides given in Table 1 to remove the X-ray eclipses for IGR J16418–4532 and IGR J16479–4514 between the orbital phase of 0.85–1.15, where phase 1.0 was chosen to be the center of the X-ray eclipse. The power spectrum of IGR J16418–4532 plotted in panel (b) of Figure 1 exhibits prominent peaks at the superorbital period of ~ 14.7 days and the second harmonic of ~ 7.4 days with an FAP of $\sim 10^{-6}$. The power spectrum of

IGR J16479–4514 plotted in panel (c) of Figure 1 exhibits a prominent peak at the superorbital period of ~ 11.9 days with an FAP of $\sim 10^{-7}$ and a smaller peak at the second harmonic of ~ 5.9 days. Removing X-ray eclipses from the light curve can cause possible aliasing effects in the power spectra of IGR J16418–4532 and IGR J16479–4514. To investigate this, the orbital intensity profiles were fit with a sinusoidal modulation with an orbital period of 3.73 days and 3.32 days for IGR J16418–4532 and IGR J16479–4514, respectively. These fitted sine curves were used to simulate light curves using the times of the Swift BAT data, and the power spectra were constructed from them. No aliasing at their superorbital modulation periods was found in the power spectra of IGR J16418–4532 and IGR J16479–4514. The refined superorbital periods of 4U 1909 + 07, IGR J16418–4532, and IGR J16479–4514 are given in Table 1.

In Figure 2 we show the Swift BAT light curves of 4U 1909 + 07, IGR J16418–4532, and IGR J16479–4514 binned with their 15.196 day, 14.702 day, and 11.894 day superorbital periods, respectively. We find no significant long-term intensity

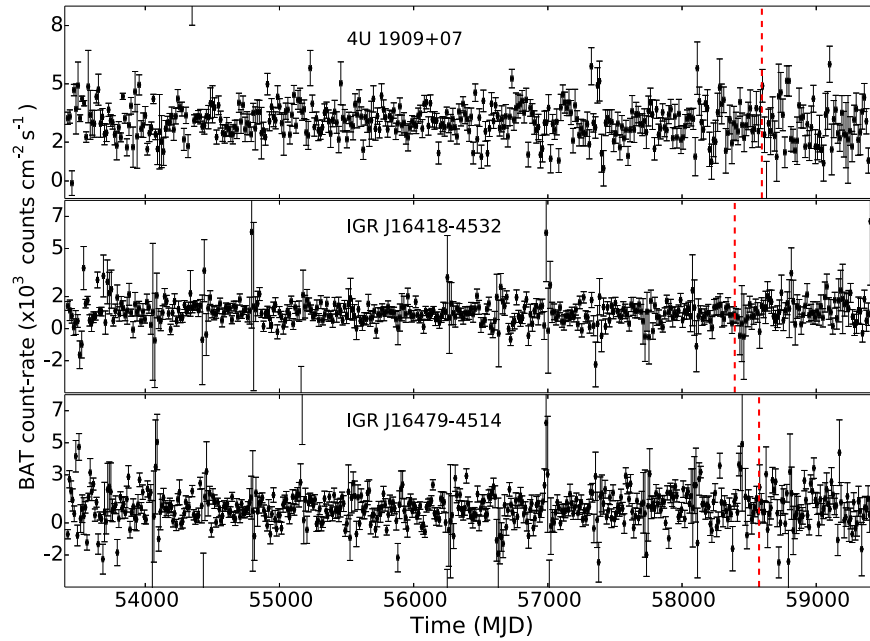


Figure 2. Swift BAT 15–50 keV light curves of 4U 1909 + 07, IGR J16418–4534, and IGR J16479–4514 binned with their superorbital periods of 15.196 days, 14.702 days and 11.894 days, respectively. The dashed red lines mark the epoch of the NuSTAR observations analyzed in this paper: MJD 58,595 for 4U 1909 + 07, MJD 58,393 for IGR J16418–4532, and MJD 58,574 for IGR J16479–4514.

variations between different superorbital cycles for any of the sources.

To monitor the changes in the strengths of the superorbital modulations, we constructed the dynamic power spectra using the Swift BAT light curves for the three sources. The power spectra were calculated using 750 day time intervals, which were successively shifted in time by 50 days relative to each other for 4U 1909 + 07, whereas for IGR J16418–4532 and IGR J16479–4514, 1000 day time intervals were used that were successively shifted in time by 50 days relative to each other. The left panels (a) of Figures 3, 4, and 5 show the dynamic power spectra constructed for the three sources using 16.7 yr of Swift BAT light curves. The red points in the left panels (b) of Figures 3, 4, and 5 show the relative height of the peak at the superorbital period to the mean power (in gray points), and the blue points show the relative height of the peak at the second harmonic to the mean power. The left panels (c) of Figures 3, 4, and 5 show the power spectra of the Swift BAT light curves, exhibiting the peaks in the power spectrum corresponding to the superorbital period and the second harmonic, along with the significance levels of the noise, similar to Figure 1, but with a smaller range of time around the superorbital period.

2.1.1. Superorbital Intensity Profiles of 4U 1909 + 07

The dynamic power spectrum of 4U 1909 + 07 shown in the left panel (a) of Figure 3 exhibits peaks at the fundamental superorbital period of ~ 15.2 days and the second harmonic of ~ 7.6 days. The strengths of these peaks vary on different timescales of years. At the epoch of the NuSTAR observations analyzed in this paper as well as the previous NuSTAR observation in 2015, the superorbital modulation at the fundamental frequency was weaker and consistent with the mean power. The mean power is defined as the average power in the power spectrum excluding any peaks and is similar to the noise. The relative height of the fundamental peak of the

superorbital period (red points) and the second harmonic (blue points) to the mean power, shown in the left panel (b) of Figure 3, is stronger by a factor of 10 or more than the mean power (gray points) during the times when the superorbital modulation at the fundamental period and/or the second harmonic was present.

To illustrate the changes in the superorbital intensity profiles associated with a change in the strength of the superorbital modulation, we divided the Swift BAT light curve into different segments where the peaks corresponding to the fundamental superorbital period and the second harmonic were stronger and/or weaker in the dynamic power spectrum. As seen in the dynamic power spectrum of 4U 1909 + 07 (left panel of Figure 3(a)), both peaks at the fundamental frequency and the second harmonic were present from MJD 53,416 to MJD 55,500, with relative heights of 10. Only the peak at the fundamental frequency was present from MJD 55,500 to MJD 56,500 with a relative height of 10. From MJD 56,500 to MJD 57,500, both the peaks at the fundamental frequency and the second harmonic were not strongly present and were consistent with the mean power. The peak at the second harmonic was present from MJD 57,500 to MJD 58,000, with the peak the fundamental frequency present briefly. Around MJD 59,500, the peak at the fundamental frequency reappeared and at the second harmonic became weaker, but continued monitoring is required to confirm this. The Swift BAT light curves were folded with the superorbital period of 15.192 days, and phase zero was chosen as the time of the maximum flux of the average superorbital intensity profile (constructed using data from MJD 53,416 to MJD 59,515) given in Table 1. The right panel of Figure 3 shows the superorbital intensity profiles constructed from these different segments of the light curve. We estimated the fractional root mean square (RMS) amplitude (f_{rms}) for the superorbital intensity profiles using the formulation in Vaughan et al. (2003). The f_{rms} for the superorbital intensity profiles is noted inside the panels

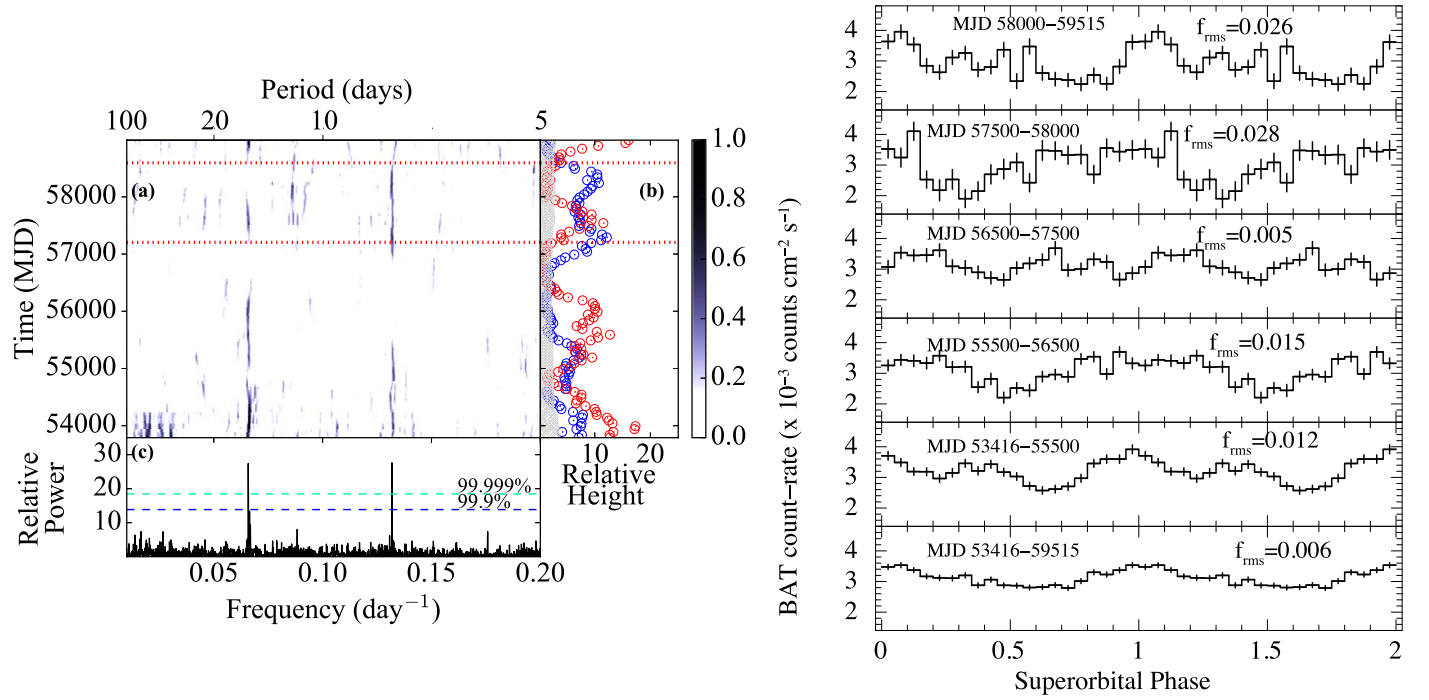


Figure 3. Left panel: panel (a) shows the dynamic power spectrum of 4U 1909 + 07 constructed using 16.7 yr of Swift BAT light curve in a 15–50 keV energy band. The power spectrum was calculated using 750 day intervals that were successively shifted in time by 50 days relative to each others. The dashed red line corresponds to the NuSTAR observations taken in 2019 analyzed in this paper. The second dashed red line corresponds to the NuSTAR observation taken in 2015. The red points in panel (b) show the relative height of the fundamental peak of the superorbital period to the mean power (in gray points), and the blue points are the relative height of the second harmonic to the mean power. Panel (c) shows the power spectrum of the Swift BAT light curve normalized to the average power, with 99.9% and 99.99% significance levels indicated by the dashed blue and green lines, respectively. Right panel: different segments of Swift BAT light curve where the peak at the fundamental and the second harmonic was stronger and/or weaker, folded on the superorbital period of 15.196 days. Phase zero was chosen as the time of the maximum flux MJD 59,502.1 \pm 0.1. The fractional RMS (f_{rms}) was calculated using the formulation of Vaughan et al. (2003) for the superorbital intensity profiles. The y-axes are plotted with the same range.

of the right plot of Figure 3. The f_{rms} was lower for the superorbital intensity profile constructed from the MJD 56,500 to MJD 57,500 when the peaks at the fundamental frequency and the second harmonic were not strongly present, compared to other segments, where at least one of the peaks was present in the dynamic power spectrum (left panel of Figure 3(a)).

2.1.2. Superorbital Intensity Profiles of IGR J16418–4532

The dynamic power spectrum of IGR J16418–4532 shown in the left panel (a) of Figure 4 exhibits peaks at the fundamental superorbital period of ~ 14.7 days and the second harmonic at ~ 7.4 days, with varying strengths on timescales of years. At the epoch of the NuSTAR observations analyzed in this paper and a previous NuSTAR observation in 2015, the superorbital modulation both at the fundamental frequency and the second harmonic was weaker and consistent with the mean power. The relative height of the fundamental peak of the superorbital period (red points) and the second harmonic (blue points) to the mean power, shown in the left panel (b) of Figure 4, is stronger by a factor of 10 or more than the mean power (gray points) during the times when the superorbital modulation at the fundamental period and/or the second harmonic was present.

To illustrate the changes in the superorbital intensity profiles associated with a change in the strength of the superorbital modulation, we excluded the X-ray eclipses in the light curve and divided the Swift BAT light curve into different segments

where the peaks corresponding to the fundamental superorbital period and the second harmonic were stronger and/or weaker in the dynamic power spectrum. As seen in the dynamic power spectrum of IGR J16418–4532 (left panel of Figure 4(a)), both peaks at the fundamental frequency and the second harmonic were present from MJD 53,416 to MJD 55,000, with relative heights of 10. Only the peak at the fundamental frequency was present with a relative height of 20 from MJD 55,000 to MJD 56,500. From MJD 56,500 to MJD 57,100, neither of the peaks at the fundamental frequency and the second harmonic were strongly present and were consistent with the mean power. Only the peak at the second harmonic was present from MJD 57,100 to MJD 58,100 with a relative height of 10. Around MJD 59,500, the peak at the fundamental frequency reappeared and at the second harmonic became weaker, but continued monitoring is required to confirm this. The Swift BAT light curves were folded with the superorbital period of 14.702 days, and phase zero was chosen as the time of the maximum flux of the average superorbital intensity profile (constructed using data from MJD 53,416 to MJD 59,515) given in Table 1. The right panel of Figure 4 shows the superorbital intensity profiles constructed from these different segments of the light curve, along with their f_{rms} . The f_{rms} was lower for the superorbital intensity profile constructed from the MJD 56,500 to MJD 57,100 when the peaks at the fundamental frequency and the second harmonic were not strongly present. The f_{rms} was highest for the superorbital intensity profile constructed from MJD 55,000 to MJD 56,500 when only the peak at the fundamental frequency was present with a relative height of 20.

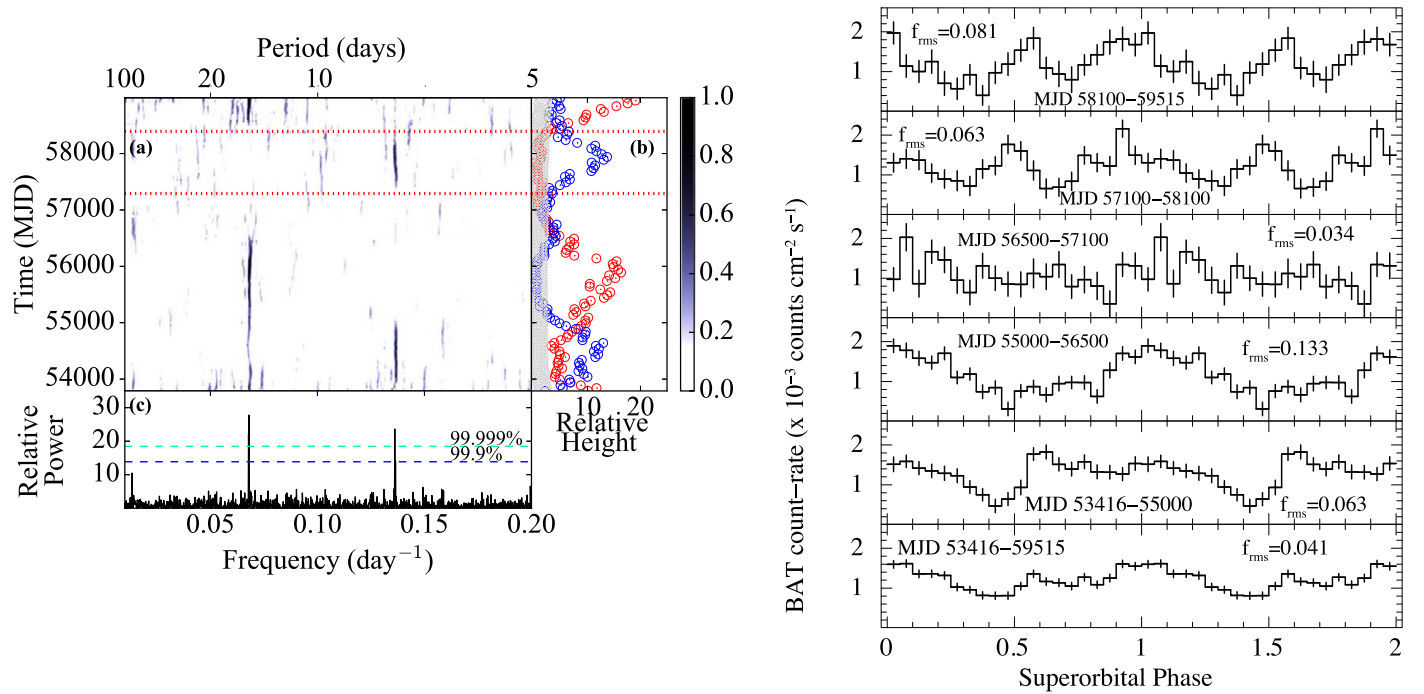


Figure 4. Left panel: panel (a) shows the dynamic power spectrum of IGR J16418–4532 constructed using 16.7 yr of the Swift BAT light curve in the 15–50 keV energy band. The power spectrum was calculated using 1000 day intervals, which were successively shifted in time by 50 days relative to each other. The dashed red line corresponds to the NuSTAR observations taken in 2018 analyzed in this paper. The second dashed red line corresponds to the NuSTAR observation taken in 2015. The red points in panel (b) show the relative height of the fundamental peak of the superorbital period to the mean power (in gray points), and the blue points are the relative height of the second harmonic to the mean power. Panel (c) shows the power spectrum of the Swift BAT light curve normalized to the average power, with 99.9% and 99.99% significance levels indicated by the dashed blue and green lines, respectively. Right panel: different segments of Swift BAT light curve where the peak at the fundamental and second harmonic were stronger and/or weaker, folded on the superorbital period of 14.702 days. Phase zero was chosen as the time of the maximum flux MJD 59,506.9 \pm 0.1. The superorbital intensity profiles were constructed excluding the X-ray eclipses in the Swift BAT light curve. The fractional RMS (f_{RMS}) was calculated using the formulation of Vaughan et al. (2003) for the superorbital intensity profiles. The y-axes are plotted with the same range.

2.1.3. Superorbital Intensity Profiles of IGR J16479–4514

From the dynamic power spectrum of IGR J16479–4514 in the left panel (a) of Figure 5, we see peaks corresponding to the fundamental of the superorbital period at ~ 11.9 days and the second harmonic at ~ 5.9 days. At the epoch of the NuSTAR observations analyzed in this paper, the superorbital modulation at both the fundamental frequency and the second harmonic were weak and consistent with the mean power. The relative height of the fundamental peak of the superorbital period (red points) and the second harmonic (blue points) to the mean power, shown in the left panel (b) of Figure 5, is stronger by a factor of 15 or more than the mean power (gray points) during the times when the superorbital modulation at the fundamental and/or the harmonic was present.

Similar to the procedure described for IGR J16418–4532, we excluded the X-ray eclipses in the light curve and divided the Swift BAT light curves into different segments where the peaks corresponding to the fundamental superorbital period and the second harmonic were stronger and/or weaker in the dynamic power spectrum. As seen in the dynamic power spectrum of IGR J16479–4514 (left plot of Figure 5(a)), both peaks at the fundamental frequency and the second harmonic were present from MJD 53,416 to MJD 56,000. Only the peak at the fundamental frequency was present from MJD 56,000 to MJD 58,000 with a relative height of 15. The Swift BAT light curves were folded with the superorbital period of 11.894 days, and phase zero was chosen as the time of the maximum flux of the average superorbital intensity profile (constructed using data from MJD 53,416 to MJD 59,515) given in Table 1. The right

panel of Figure 5 shows the superorbital intensity profiles constructed from these different segments of the light curve, along with their f_{rms} . The f_{rms} was lower for the superorbital intensity profile constructed from the MJD 58,000 to MJD 59,515 when the peaks at the fundamental frequency and the second harmonic were not strongly present and were consistent with the mean power.

For IGR J16418–4532 and IGR J16479–4514, other peaks are seen in the dynamic power spectra that are not related to either the orbital or superorbital modulations (panel (a) of the left plots of Figures 4 and 5). However, none of the peaks have a high statistical significance as the fundamental frequency of the superorbital modulation or the second harmonic. The dynamic power spectrum was calculated using a 1000 day sliding window, shifted by 50 days, and the modulations at these periods lasted for shorter durations than the more prominent superorbital modulation. As seen in panel (c) of the left plots of Figures 4 and 5, the statistical significance of these short peaks are lower than statistical significance levels of 99.9% and 99.99% and have an FAP of $\sim 10^{-1}$. These peaks are therefore most likely spurious and might be due to statistical noise.

2.2. Pointed Observations with Swift XRT and NuSTAR

2.2.1. NuSTAR

NuSTAR is a hard X-ray telescope operating in the 3–79 keV energy band (Harrison et al. 2013). It carries two coaligned grazing-incidence Wolter I imaging telescopes that focus onto two independent focal plane modules, FPMA and

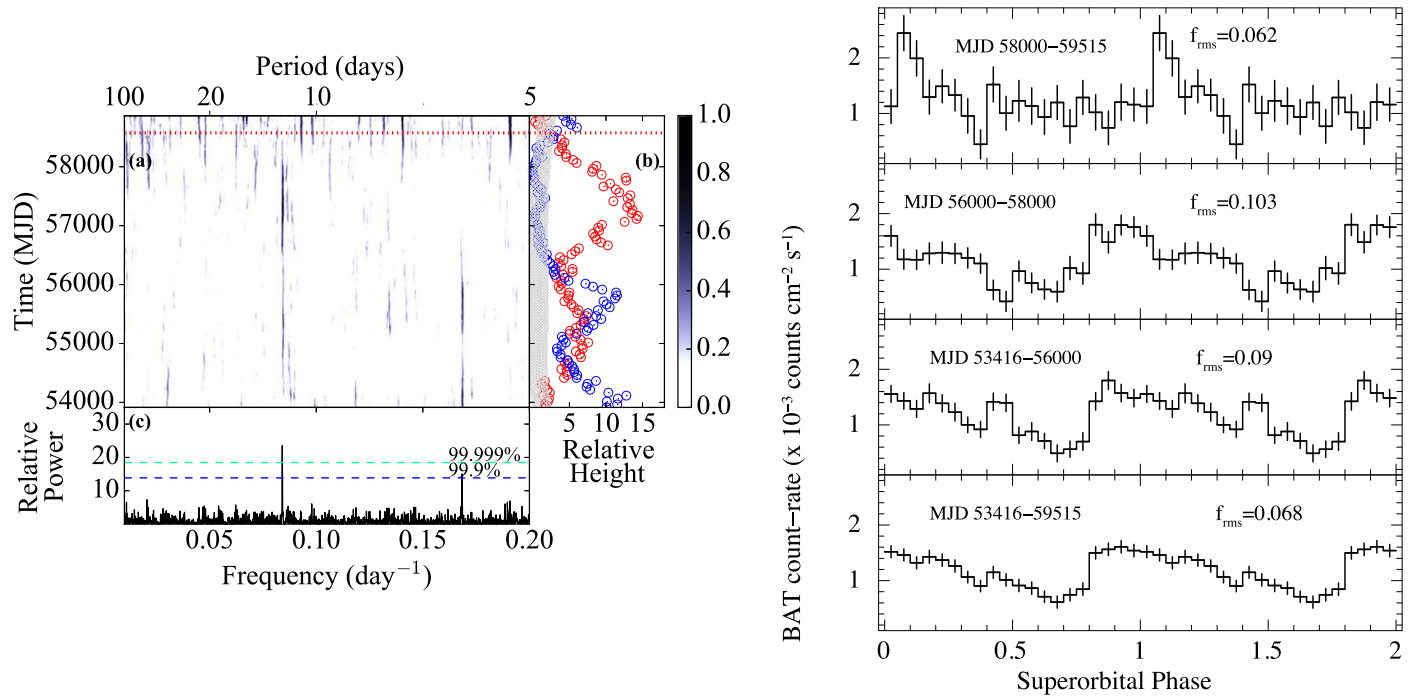


Figure 5. Left panel: panel (a) shows the dynamic power spectrum of IGR J16479–4514 constructed using 16.7 yr of Swift BAT light curve in a 15–50 keV energy band. The power spectrum was calculated using 1000 day intervals, shifted in time by 50 days relative to each other. The dashed red line corresponds to the NuSTAR observations taken in 2019 analyzed in this paper. The red points in panel (b) show the relative height of the fundamental peak of the superorbital period to the mean power (in gray points), and the blue points are the relative height of the second harmonic to the mean power. Panel (c) shows the power spectrum of the Swift BAT light curve normalized to the average power, with 99.9% and 99.99% significance levels indicated by the dashed blue and green lines, respectively. Right panel: different segments of Swift BAT light curve where the peak at the fundamental and second harmonic was stronger and/or weaker, folded on the superorbital period of 11.894 days. Phase zero was chosen as the time of the maximum flux $\text{MJD } 59,507.7 \pm 0.1$. The superorbital intensity profiles were constructed excluding the X-ray eclipses in the Swift BAT light curve. The fractional RMS (f_{RMS}) was calculated using the formulation of Vaughan et al. (2003) for the superorbital intensity profiles. The y-axes are plotted with the same range.

FPMB. The NuSTAR observations were performed around the predicted superorbital maximum and minimum of a single superorbital cycle for the three sources according to the superorbital phase ephemerides given in Corbet & Krimm (2013). In addition to the NuSTAR observations, Swift XRT observations with short exposures (~ 2 ks) were simultaneously carried out, except for the NuSTAR observations of 4U 1909+07 during its predicted superorbital maximum phase. Table 2 gives a summary of the NuSTAR and Swift XRT observations for the three sources that are analyzed in this paper, along with their predicted superorbital and orbital phase.

The NuSTAR data were reduced and analyzed using NuSTAR Data Analysis Software (NuSTARDAS) v.2.1.1 package provided under *HEASoft* v.6.29 and calibration files 2021-10-26. The event files were reprocessed using *nupipeline* using the standard filtering procedure and the default screening criteria. The event times were corrected to the solar system barycenter using *nuproducts* and the *FTOOL* *barycorr* with the DE200 solar system ephemeris. The source spectra, response matrices, ancillary matrices, and energy-resolved light curves were extracted in SCIENCE mode (01) from a circular region of radius $60''$ centered on the source using *nuproducts*. The background spectra and light curves were extracted from a circular region of $60''$ in a source-free region on the same chip. To carry out the analysis with user-input good-time intervals especially for the analysis of the X-ray flares in the light curves of 4U 1909+07 and IGR J16418–4532, we use *usrgti* as an input to *nuproducts*. We corrected the event times for the orbital motion of the NS in 4U 1909+07 using the ephemerides given in

Levine et al. (2004) for a circular orbit. Since the orbital ephemerides of IGR J16418–4532 and IGR J16479–4514 are unknown, we do not correct the event files for the orbital motion of the compact object.

2.2.2. Swift XRT

Swift XRT is a Wolter I imaging telescope sensitive to X-rays ranging from 0.3 to 10 keV (Burrows et al. 2005). The data were reduced and analyzed with *HEASoft* v.6.29 and calibration files 20210915. The event files were reprocessed using *xrtpipeline* using the standard filtering procedure and the default screening criteria.⁹ We used the observations in photon-counting (PC) mode, applying the standard filtering procedures. The Swift XRT observation of 4U 1909+07 carried out at the predicted superorbital minimum phase has a moderate pileup. To mitigate the effects of the pileup, we used the pileup threads given in the XRT analysis guide.¹⁰ The source region was taken as an annulus with an outside radius of $60''$ and an inner radius of $7''$. The background spectrum was extracted from a circular region of radius $60''$ from a source-free region.

The Swift XRT observations of IGR J16418–4532 and IGR J16479–4514 were not affected by pileup. The source spectra were extracted from a circular region of radius $60''$ centered on the source and background spectra were extracted with the same radius from a source-free region. The exposure maps and

⁹ <https://www.swift.ac.uk/analysis/xrt/>

¹⁰ <https://www.swift.ac.uk/analysis/xrt/pileup.php>

Table 2
Summary of X-Ray Observations

Source	Telescope	ObsID	Start Time	End Time	Orbital Phase	Superorbital Phase	Total Exposure (ks)	Avg Count Rate (3–50 keV)
4U 1909 + 07	NuSTAR	30402026002	2019-04-22T00:11:09	2019-04-22T11:36:09	0.37–0.48	0.68–0.71	18.8	4.7(FPMA)/4.5(FPMB)
	Swift XRT	00088747001	2019-04-22T01:04:34	2019-04-22T02:53:52	0.4	0.7	1.8	0.64
	NuSTAR	30402026004	2019-04-26T13:41:09	2019-04-27T20:56:09	0.41–0.52	0.98–1.02	23.2	6.9(FPMA)/6.6(FPMB)
IGR J16418–4532	NuSTAR	30402027002	2018-10-02T20:51:09	2018-10-03T07:51:09	0.84–0.96	0.88–0.91	19.85	0.59(FPMA)/0.55(FPMB)
	Swift XRT	00088748001	2018-10-02T21:32:47	2018-10-02T23:25:52	0.85	0.89	1.8	0.13
	NuSTAR	30402027004	2018-10-10T18:51:09	2018-10-11T12:21:09	0.96–1.15	1.42–1.4	31.02	1.2(FPMA)/1.1(FPMB)
IGR J16479–4514	Swift XRT	00088748002	2018-10-10T20:45:56	2018-10-10T22:39:52	0.98	1.44	1.8	0.24
	NuSTAR	30402028002	2019-04-01T19:06:09	2019-04-02T07:36:09	0.49–0.65	0.07–0.11	21.86	1.5(FPMA)/1.4(FPMB)
	Swift XRT	00088749001	2019-04-01T20:28:34	2019-04-01T22:21:53	0.55	0.095	1.9	0.30
	NuSTAR	30402028004	2019-04-09T09:11:09	2019-04-10T15:07:18	0.78–0.98	0.71–0.76	31.02	2.3(FPMA)/2.1(FPMB)
	Swift XRT	00088749002	2019-04-09T10:11:19	2019-04-09T12:13:54	0.8	0.73	1.9	0.06

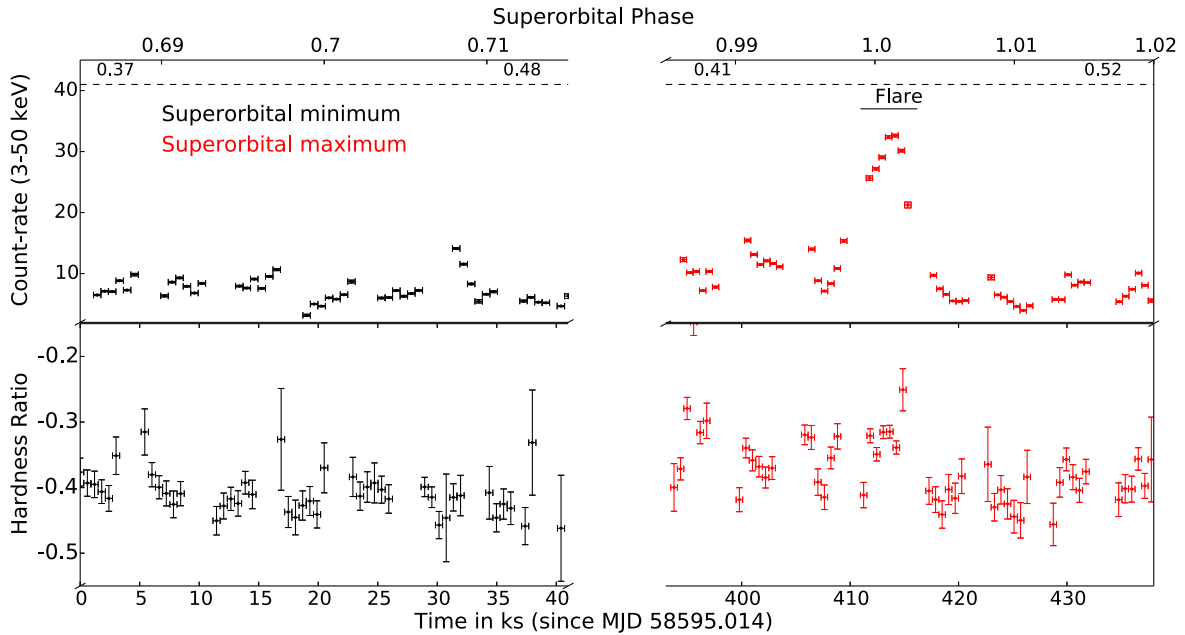


Figure 6. NuSTAR FPMA+FPMB light curves of 4U 1909 + 07 in 3–50 keV energy band, binned with the pulsar spin period of 603 s. The hardness ratios were constructed using light curves in 3–10 keV and 10–50 keV. The top x-axis displays the superorbital phase of the observations calculated using the ephemerides given in Corbet & Krimm (2013). The dashed line on the top x-axis displays the orbital phase of the observations calculated using the ephemerides given in Levine et al. (2004). The red points correspond to the observation carried out during the predicted superorbital maximum phase, and the black points correspond to the observation carried out during the predicted superorbital minimum phase. The segment “flare” denotes a short X-ray flare in the observation when the count rate increased by a factor of 5.

ancillary response matrices were extracted using `xrtexpo-map` and `xrtmkarf`, respectively.

The NuSTAR and Swift XRT source spectra were grouped to give a minimum of 30 counts in each spectral bin. In addition to the ObsIDs listed in Table 1, we also used an archival NuSTAR observation (ObsID:30101036002, obs date:2015-09-26) and an archival XMM-Newton observation (ObsID:0823990401, obs date:2019-02-21) of IGR J16418–4532 to investigate the long-term behavior of the source. The NuSTAR observation was analyzed using the same procedure as mentioned in Section 2.2.1. The XMM-Newton observation was carried out in full-window-imaging mode and was analyzed using SAS v19.1.0 with the latest calibration files. The light curves were extracted using the XMM-SAS data analysis threads,¹¹ which filtered out the background flares and applied the latest calibration files. A circular source region was selected with a radius of 40'' centered on the source, and a similar size background region was selected in a source-free region on the chip. This XMM observation was used to study the spin period of the source, hence only EPIC-PN data were used.

2.2.3. Light Curves and Hardness Ratios

The energy-resolved light curves of the NuSTAR observations were constructed in 3–50 keV, 3–10 keV, and 10–50 keV energy bands to study the short-term variability and changes in hardness ratio during an observation. The hardness ratio is defined for the light curves in the energy ranges 3–10 keV (with count rate C_S) and 10–50 keV (with count rate C_H) as

$$\text{HR} = \frac{C_H - C_S}{C_H + C_S}. \quad (1)$$

Figure 6 shows the NuSTAR FPMA+FPMB light curves in the 3–50 keV energy band of the two 4U 1909 + 07 observations, binned with the pulsar spin period of 603 s. There is a short 3 ks X-ray flare marked as “flare” around superorbital phase ~ 1.0 and orbital phase of ~ 0.5 , where the count rate increases by a factor of 5. This short X-ray flare is most likely related to a short-term variability arising due to accretion from a clumpy stellar wind. To disentangle this short-term variability from the superorbital modulations, we remove the short X-ray flare from the pulse profiles and spectral analysis and focus only on the nonflaring part of the observations. With the exception of the short X-ray flare, the count rate remains similar for both observations, which is indicative of the weakened amplitude of the superorbital modulations seen with Swift BAT in the left panel of Figure 3(a). We find no significant change in the hardness ratios between the predicted superorbital maximum and minimum observations.

In Figure 7, the NuSTAR FPMA+FPMB 3–50 keV energy band light curves of IGR J16418–4532 were binned with 302 s, one-fourth of the spin period of the pulsar (1208 s), to show several short X-ray flares during which the count rate increases by a factor of 5–10. The hardness ratios suggest a spectral softening during these X-ray flares. There are several shorter X-ray flares in the predicted superorbital minimum observation compared to that present in the predicted superorbital maximum observation, likely due to the longer duration of the observation. This could also explain the higher X-ray fluxes seen in Table 3 for the observation at the predicted superorbital minimum phase, compared to that of the observation at the predicted superorbital maximum phase.

Figure 8 shows the NuSTAR FPMA+FPMB 3–50 keV energy band light curves of IGR J16479–4514, binned with 500 s. We see two large X-ray flares in the light curve: at superorbital phase ~ 0.08 (orbital phase of ~ 0.5), where the

¹¹ <https://www.cosmos.esa.int/web/xmm-newton/sas-threads>

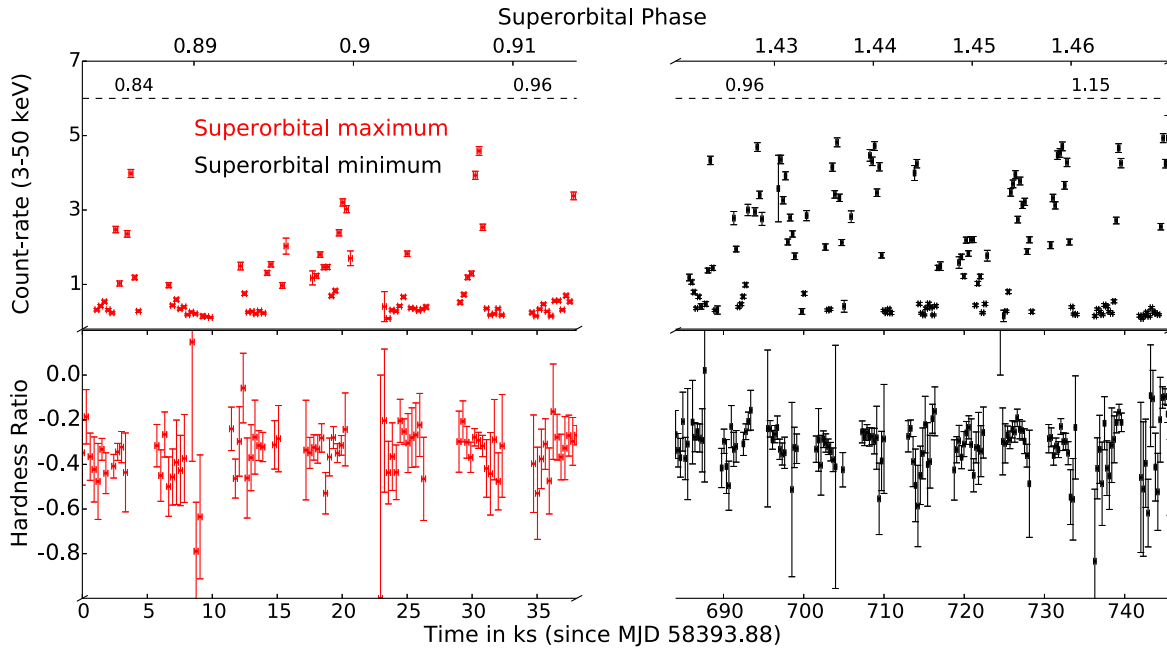


Figure 7. NuSTAR FPMA+FPMB light curves of IGR J16418–4532 in 3–50 keV energy band, binned with 302 s, one-fourth of the spin period of the pulsar (1208 s). The hardness ratios were constructed using light curves in 3–10 keV and 10–50 keV. The top x-axis displays the predicted superorbital phase of the observations calculated using the ephemerides given in Corbet & Krimm (2013). The dashed line on the top x-axis displays the orbital phase of the observations calculated using the ephemerides given in Coley et al. (2015). The red points correspond to the observation carried out during the predicted superorbital maximum phase, and the black points correspond to the observation carried out during the predicted superorbital minimum phase.

count rate increases by a factor of 10 (Figure 8(a)), and at superorbital phase ~ 0.74 (orbital phase of ~ 0.9), where the count rate increases by a factor of 100 (Figure 8(b)). These large X-ray flares are most likely related to the orbital phase-locked X-ray flares previously detected in this system (Sidoli et al. 2012; Sguera et al. 2020). To disentangle the effects of the orbital phase-locked matter in a clumpy stellar wind from the long-term variability from the superorbital modulations, we remove these large X-ray flares from the spectral analysis and focus only on the nonflaring part of the observations. The nonflaring part of the light curve in Figure 8(c) exhibits small fluctuations in the count rates. The average count rate in the nonflaring part of the light curve is similar for both observations. The hardness ratios suggest that the spectral shape softens during the X-ray flares and remains constant outside the flares.

2.2.4. Pulsations and Energy-resolved Pulse Profiles

To search for the pulsations in the NuSTAR observations of the three sgHMXBs, we used the epoch-folding and χ^2 maximization techniques using the FTOOL *efsearch* (Leahy 1987) on the light curves binned with 1 s. The errors on the pulse periods are estimated for a 1σ confidence interval. The pulsation search was carried out separately for the two NuSTAR observations of 4U 1909+07. The pulse period of the NS for the predicted superorbital minimum observation is 602.9 ± 0.1 s, and for the predicted superorbital maximum observation, it is 603.2 ± 0.1 s. For IGR J16418–4532, we combined the light curves from both observations and calculated the pulse period to be 1208.6 ± 0.1 s. To evaluate the long-term pulse period changes in IGR J16418–4532, we estimate the pulse periods from a previous NuSTAR observation carried out in 2015 and an XMM observation in 2019 from their light curves

binned with 1 s. The pulse period estimated from the 2015 NuSTAR observation is 1209.2 ± 0.1 s, and from the XMM observation, it is 1207.9 ± 0.2 s.

Pulsations have not been detected previously in IGR J16479–4514. To search for pulsations in the NuSTAR light curves, we used the χ^2 maximization technique using FTOOLS *efsearch*, power spectrum *powspec*, and a Lomb–Scargle periodogram (Scargle 1982). We separately checked for pulsations in the large X-ray flares and the nonflaring part of the light curves, but did not find any. The tentative spin-period range estimated from its position on the P_{spin} versus P_{orbital} Corbet diagram is 500–1000 s (Corbet 1986). Since the large X-ray flares last around 3 ks, which would be a few pulse period cycles, we only use the nonflaring part to estimate the upper limit on the pulse fraction. We folded the 3–50 keV NuSTAR light curves of IGR J16479–4514 for the nonflaring part with 500–1000 s as the tentative spin period with 1 s steps, and estimated the upper limit on the pulse fraction for the putative NS as 16%.

To investigate the energy dependence of the pulse profiles for 4U 1909+07 and IGR J16418–4532, we extracted the light curves from the NuSTAR observations in energy bands of 3–6 keV, 6–10 keV, 10–20 keV, 20–30 keV, and 30–50 keV and folded them with their estimated pulse periods to create the energy-resolved pulse profiles. The energy-resolved pulse profiles created from the predicted superorbital minimum and maximum observations are overlaid on the same plot to compare any changes in the shape of the pulse profiles. The peak of the pulse profiles was aligned to phase 0 for the pulse profiles in the 3–50 keV energy band.

The energy-resolved pulse profiles for 4U 1909+07 for both the NuSTAR observations (excluding the short X-ray flare) are shown in the left panel of Figure 9. The energy-resolved pulse profiles below 20 keV are quasi-sinusoidal with a primary peak at phase 0, a dip around phase 0.8, and a

Table 3

Best-fitting Parameter Values for the Swift XRT + NuSTAR Spectra of 4U 1909 + 07 Using the Models Defined in Section 2.3 for the Observations at the Predicted Superorbital Minimum and Maximum Phases, and the X-Ray Flare

Parameters	HIGHECUT			CUTOFFPL			NPEX		
	Min	Max	Flare	Min	Max	Flare	Min	Max	Flare
C_{XRT}	1.11 ± 0.06	1.12 ± 0.06	1.11 ± 0.06
C_{FPMB}	1.04 ± 0.01	1.03 ± 0.01	1.02 ± 0.01	1.04 ± 0.01	1.03 ± 0.01	1.02 ± 0.01	1.04 ± 0.01	1.03 ± 0.01	1.03 ± 0.01
N_{H}^a	7.2 ± 0.4	$6.9^{+0.5}_{-0.7}$	5.9 ± 0.6	7.9 ± 0.4	7.3 ± 0.5	6.3 ± 0.6	6.7 ± 0.3	6.0 ± 0.4	5.5 ± 0.6
Γ	1.51 ± 0.04	$1.4^{+0.05}_{-0.1}$	1.20 ± 0.06	1.34 ± 0.04	1.20 ± 0.05	0.92 ± 0.06	0.90 ± 0.05	$0.81^{+0.08}_{-0.06}$	0.63 ± 0.04
Norm ^b	4.2 ± 0.4	3.7 ± 0.5	9 ± 1	4.3 ± 0.3	3.5 ± 0.3	7.8 ± 0.8	2.7 ± 0.2	2.2 ± 0.2	5.7 ± 0.5
Cutoff energy E_{C}^c	7.8 ± 0.4	$8.1^{+0.5}_{-1.0}$	8.4 ± 0.4
Fold energy E_{F}^c	24 ± 1	26 ± 2	20 ± 1	19 ± 1	20 ± 1	15.3 ± 0.9	$8.9^{+0.9}_{-0.6}$	$9.9^{+1.5}_{-0.9}$	9.7 ± 0.2
Fe K α ^c	6.35 ± 0.06	6.35 ± 0.04	6.38 ± 0.05	6.39 ± 0.05	6.37 ± 0.04	6.40 ± 0.05	6.38 ± 0.05	6.35 ± 0.04	6.39 ± 0.05
Fe K β ^c	7.1 ± 0.2	6.9 ± 0.2	7.0 ± 0.3	7.5 ± 0.2	7.1 ± 0.2	7.2 ± 0.2	7.5 ± 0.3	6.9 ± 0.2	7.1 ± 0.3
Fe K α Norm ^d	1.8 ± 0.3	2.9 ± 0.4	9 ± 2	1.8 ± 0.3	2.9 ± 0.3	8 ± 2	1.7 ± 0.3	2.9 ± 0.4	8 ± 1
Fe K β Norm ^d	0.7 ± 0.3	0.6 ± 0.4	2 ± 1	1.0 ± 0.3	0.8 ± 0.3	3 ± 1	0.8 ± 0.3	0.7 ± 0.3	2 ± 1
Fe K α EW ^e	69 ± 13	109 ± 15	94 ± 15	70 ± 12	108 ± 13	88 ± 17	66 ± 12	108 ± 13	87 ± 17
Fe K β EW ^e	32 ± 14	27 ± 17	22 ± 17	58 ± 13	34 ± 13	29 ± 16	38 ± 13	29 ± 15	23 ± 16
χ^2_{ν}/dof	$1.11/318$	$0.91/246$	$1.01/246$	$1.2/308$	$1.13/247$	$1.23/247$	$1.16/307$	$0.93/246$	$1.09/247$
Flux _s ^f	1.26 ± 0.03	1.27 ± 0.01	1.27 ± 0.01
Flux _h ^g	4.06 ± 0.02	4.99 ± 0.03	18.1 ± 0.1	4.03 ± 0.02	4.90 ± 0.03	17.8 ± 0.1	4.07 ± 0.02	4.96 ± 0.03	18.0 ± 0.1

Notes. The errors on the parameters are estimated using 90% confidence limits.^a in units of 10^{22} cm^{-2} .^b in units of $10^{-2} \text{ photons keV}^{-1} \text{ cm}^2 \text{ s}^{-1}$ at 1 keV.^c in units of keV^d in units of $10^{-4} \text{ photons cm}^2 \text{ s}^{-1}$.^e EW is the equivalent width in units of eV.^f unabsorbed X-ray flux in 0.5–8.0 keV in $10^{-10} \text{ erg s}^{-1} \text{ cm}^{-2}$.^g Unabsorbed X-ray flux in 3–70 keV in $10^{-10} \text{ erg s}^{-1} \text{ cm}^{-2}$.

broader secondary peak around 0.5. At energies above 20 keV, the profile changes to a single-peak sinusoidal profile. The shape of these energy-resolved pulse profiles is similar for both observations. The pulse profiles are similar to those seen in previous studies with RXTE (Fürst et al. 2011), Suzaku (Fürst et al. 2012; Jaisawal et al. 2013), NuSTAR, and AstroSat (Jaisawal et al. 2020).

The energy-resolved pulse profiles of IGR J16418–4532 in the right panel of Figure 9 exhibit a considerable difference between the pulse profiles observed at the predicted superorbital minimum and maximum observations, especially at lower energies. The energy-resolved pulse profiles are complex at energies below 20 keV; the superorbital minimum pulse profile shows a narrow dip at phase 0.5 and two peaks at phase 0 and 0.8, whereas the narrow dip and the peak at phase 0.8 is absent in predicted superorbital maximum observation. At energies above 20 keV, the pulse profile changes to a single-peak sinusoidal profile.

The pulse fraction is defined as

$$\text{PF} = \frac{F_{\text{max}} - F_{\text{min}}}{F_{\text{max}} + F_{\text{min}}}, \quad (2)$$

where F_{max} and F_{min} are the maximum and minimum count rate in the pulse profiles, respectively. Figure 10 shows the energy dependence of the pulse fraction for the energy-resolved pulse profiles of 4U 1909 + 07 and IGR J16418–4532 for the NuSTAR observations, which increase as a function of energy for both observations.

2.3. Broadband Spectral Analysis

The simultaneous broadband fitting of the Swift XRT and the NuSTAR spectra of the three sources was carried out using empirical spectral models often used for fitting HMXB pulsars: a power law with high-energy cutoff (HIGHECUT, White et al. 1983), a power law with high-energy exponential cutoff (CUTOFFPL), a power law with a Fermi–Dirac cutoff (FDCUT, Tanaka 1986), and negative and positive power-law exponential (NPEX, Mihara 1995). Different spectral models were used to fit the same spectra to check for the consistency of the results. All spectral models were modified by a photoabsorption component that fully covers the source tbabs in XSPEC using verner cross sections and aspl abundances (Verner et al. 1996; Wilms et al. 2000; Asplund et al. 2009). The cross-calibration constants normalized to NuSTAR/FPMA were convolved with the above spectral models to account for the instrumental calibration uncertainties. The X-ray fluxes and their errors were estimated using the cflux model in XSPEC. All spectral fits were carried out using XSPEC v 12.12.0.

2.3.1. Pulse-phase-averaged Spectral Analysis of 4U 1909 + 07

For 4U 1909 + 07, a Swift XRT observation was performed simultaneously with the NuSTAR observation for only the predicted superorbital minimum phase. Therefore, we fitted the Swift XRT + NuSTAR spectra for the predicted superorbital minimum observation, only NuSTAR spectra for the predicted superorbital maximum observation (excluding the X-ray flare), and the short X-ray flare separately with the spectral models described in Section 2.3. The energy band chosen for spectral fitting for Swift XRT is 0.5–8.0 keV, and NuSTAR FPMA and

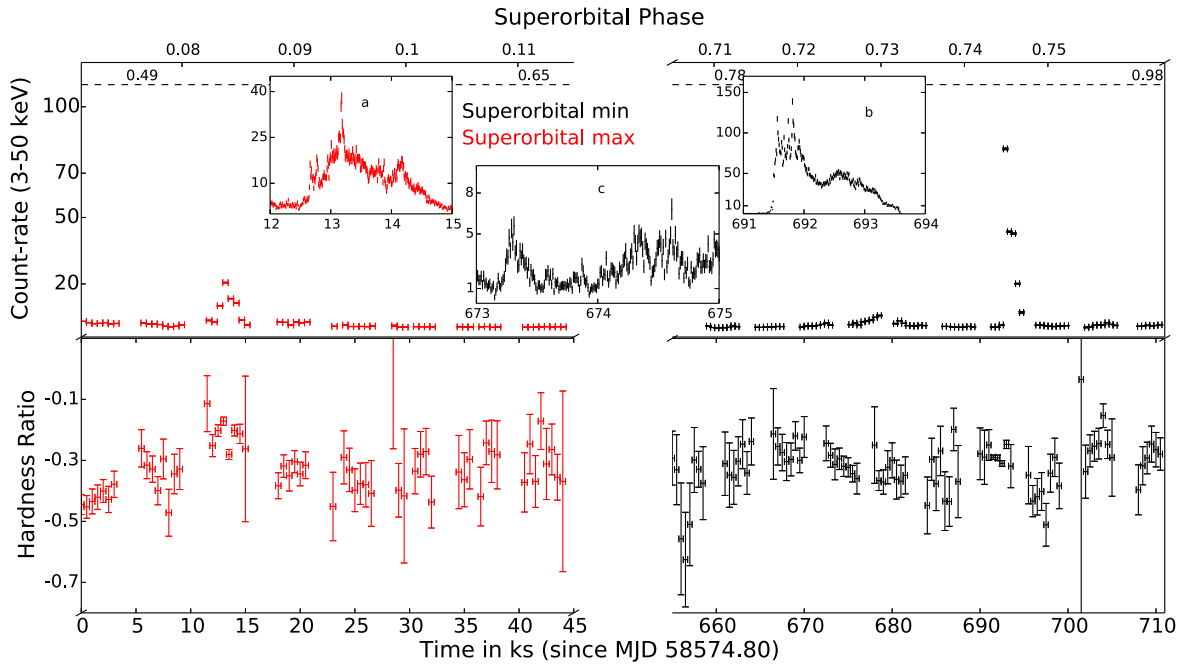


Figure 8. NuSTAR FPMA+FPMB light curves of IGR J16479–4514 in 3–50 keV energy band, binned by 500 s. The hardness ratios were constructed using light curves in 3–10 keV and 10–50 keV. The top x -axis displays the predicted superorbital phase of the observations calculated using the ephemerides given in Corbet & Krimm (2013). The dashed line on the top x -axis displays the orbital phase of the observations calculated using the ephemerides given in Coley et al. (2015). The red points correspond to the observation carried out during the predicted superorbital maximum phase, and the black points correspond to the observation carried out during the predicted superorbital minimum phase. The inset plot (a) displays an enlarged view of the X-ray flare at the superorbital phase 0.08, (b) displays an enlarged view of the X-ray flare at the superorbital phase 0.74, and (c) displays an enlarged view of the nonflaring part of the light curve. The inset plots are binned with 10 s.

FPMB are 3.0–70.0 keV. Fe fluorescence lines are seen in the spectra at 6.4 keV and 7.1 keV, which were modeled by Gaussian lines. The widths of the Gaussian lines for the 6.4 keV Fe $K\alpha$ and 7.1 keV Fe $K\beta$ lines were fixed at 0.1 keV. The errors on the equivalent widths of the Gaussian lines were propagated from their line fluxes. The spectral parameters especially the cutoff energy E_C cannot be constrained to a feasible value using the spectral model FDCUT, and hence we report results of the spectral fits using the spectral models CUTOFFPL, HIGHECUT, and NPEX in Table 4. The error bars are reported at the 90% confidence limit. Figure 11 shows the spectral fit to the pulse-phase-averaged spectra for the predicted superorbital minimum, maximum observations, and the X-ray flare along with the residuals to the best fit to the HIGHECUT, CUTOFFPL, and NPEX model for 4U 1909 + 07.

2.3.2. Pulse-phase-averaged Spectral Analysis of IGR J16418–4532

For IGR J16418–4532, the background dominates above 60 keV and was therefore chose to fit the Swift XRT and NuSTAR spectra in the 0.5–8.0 keV and 3.0–60.0 keV energy bands, respectively. The broadband Swift XRT and NuSTAR spectra of the predicted superorbital minimum and maximum observations were fit with the four spectral models described in Section 2.3: CUTOFFPL, HIGHECUT, NPEX, and FDCUT. A Gaussian line was used to model the 6.4 keV Fe $K\alpha$ line present in the spectra for the predicted superorbital minimum observation, and its width was fixed at 0.1 keV. There were no strong residuals around the 6.4 keV Fe $K\alpha$ line while fitting the predicted superorbital maximum spectra with the four spectral models. We model a Gaussian line with a fixed line center at 6.4 keV and fit the spectra to estimate the upper limits on the equivalent width and the line flux of the Fe $K\alpha$ line, which is reported in Table 3. In the bottom right panel of Figure 12, the

NuSTAR observation of IGR J16418–4532 at the predicted superorbital minimum phase shows absorption-like features around ~ 50 keV for residuals to the spectral fits with CUTOFFPL, HIGHECUT, and NPEX models. These absorption-like negative features are not seen in the residuals to the spectral fits to the FDCUT model. These negative absorption-like residuals were fit with an absorption line with a Gaussian optical depth profile gabs model, and the spectral parameters are reported in Table 3. To determine the significance of the inclusion of the possible absorption feature, we carried out simftest in XSPEC, which simulates 10^4 iterations of the spectra based on the actual data and tests the resulting $\Delta\chi^2$ using an additional model component (absorption line gabs here; Protassov et al. 2002). The statistical significance of this absorption feature is low $\leq 25\%$, which suggests that the improvement of the spectral fit by adding an absorption feature to the spectral model is negligible.

The NuSTAR observation at the predicted superorbital maximum does not exhibit any absorption-like negative residuals in the spectral fits (top panel of Figure 12), most likely due to the shorter observation time of 20 ks as compared to 31 ks of the predicted superorbital minimum observation. To further investigate these absorption-like features in the spectra of IGR J16418–4532, we analyzed a 40 ks NuSTAR observation carried out on MJD 57,291 (2015-09-26). The NuSTAR data were extracted with the same procedure as described in Section 2.2.1. The energy band chosen for fitting the spectra was 3.0–60 keV because the contribution from the background dominates above 60 keV. We fit the 2015 NuSTAR FPMA and FPMB spectra simultaneously with the four spectral models CUTOFFPL, HIGHECUT, NPEX, and FDCUT. A 6.4 keV Fe $K\alpha$ line was present in the spectrum, which was modeled by a Gaussian line. The bottom right panel

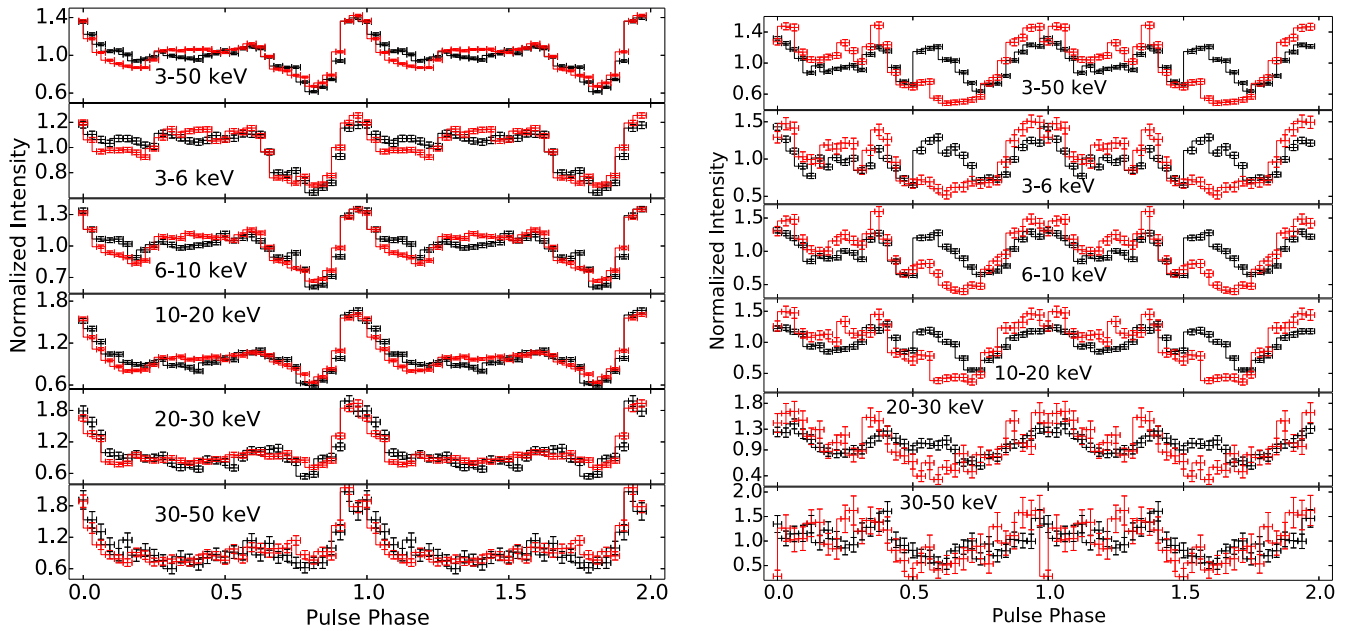


Figure 9. Energy-resolved pulse profiles created with NuSTAR FPMA+FPMB light curves of 4U 1909 + 07 (left panel) and IGR J16418–4532 (right panel). The pulse profiles for the predicted superorbital minimum (black lines) and maximum (red lines) observations are overlaid on the same plot for comparison.

of Figure 12 shows the best fit to the spectra for the 2015 NuSTAR observation along with the residuals to the best fit for the HIGHECUT, CUTOFFPL, NPEX, and FDCUT model. We see a negative absorption-like residual in the best fit for models HIGHECUT, CUTOFFPL, and NPEX in spectra at ~ 50 keV, similar to that seen for the predicted superorbital minimum observation, whereas no such residuals were seen with the FDCUT model. These negative absorption-like features were fit with an absorption line with a Gaussian optical depth *gabs* model, and the spectral parameters are reported in Table 3. From a similar analysis using *simftest*, we found that the statistical significance of this absorption feature is $\leq 47\%$ for the spectral fits to the 2015 observation, which is an improvement over the statistical significance of the absorption feature to the spectral fits for the predicted superorbital minimum observation in 2018. However, we cannot conclusively confirm or rule out a cyclotron-scattering resonance feature (CRSF) in the spectrum, which could be a possible explanation for these negative absorption-like features in the residuals to the spectral fits.

2.3.3. Pulse-phase-averaged Spectral Analysis of IGR J16479–4514

The light curves of IGR J16479–4514 show large X-ray flares, one at the superorbital phase ~ 0.08 and the other at ~ 0.7 . We exclude the X-ray flares and extract the spectrum from the nonflaring part of the light curve to investigate the difference in the spectral parameters between the nonflaring part of the superorbital phases, which could be related to the mechanisms driving the superorbital modulation. We note that the Swift XRT observation contemporaneous with the NuSTAR observations at the predicted superorbital minimum phase had a low X-ray count rate ($0.03 \text{ counts s}^{-1}$, given in Table 2) and hence, this Swift XRT observation was not used for the broadband spectral fitting. We use the spectral models HIGHECUT, CUTOFFPL, and NPEX to fit the spectra from the nonflaring part of the NuSTAR light curves. The contribution from the background dominates

above 40 keV for the NuSTAR spectra, and therefore, we chose to fit the Swift XRT and NuSTAR spectra in the 0.5–8.0 keV and 3.0–40.0 keV energy bands, respectively. The spectral model FDCUT was unable to constrain the cutoff energy (E_{cut}) of the spectra, and hence, we do not use this model for the spectral fitting. We report results from the spectral fits to the nonflaring part of the predicted superorbital minimum and maximum observations in Table 5. The cross-normalization constant between Swift XRT and NuSTAR is large, which could be due to the intrinsic source variability between the Swift XRT and NuSTAR observations. Figure 13 shows the spectral fits to the phase-average spectra for the nonflaring part of light curves of the predicted superorbital minimum and maximum observation, along with the residuals to the best fit to the HIGHECUT, CUTOFFPL, and NPEX model for IGR J16479–4514. A detailed analysis of the large X-ray flares will be presented in a separate paper.

2.3.4. Pulse-phase-resolved Spectral Analysis of 4U 1909 + 07 and IGR J16418–4532

We carried out a pulse-phase-resolved spectroscopic analysis of NuSTAR observations of 4U 1909 + 07 and IGR J16418–4532 to investigate the dependence of the spectral parameters as a function of the pulse phase. The phase bins were chosen to be 0.1 of the pulse period, and the NuSTAR spectra were extracted for 10 independent pulse phases. Since the exposures of the Swift XRT observations were short, we did not use them for the pulse-phase-resolved analysis. For 4U 1909 + 07, we model the pulse-phase-resolved spectra with a HIGHECUT model modified by an absorption component, along with a Gaussian line to model the Fe $K\alpha$ fluorescence line. There were no strong residuals around the Fe $K\beta$ line at 7.1 keV while fitting the pulse-phase-resolved spectra with HIGHECUT model, and hence, we fix this line to its pulse-phase-averaged spectral values mentioned in Table 4. The results of the pulse-phase-resolved spectral study for the

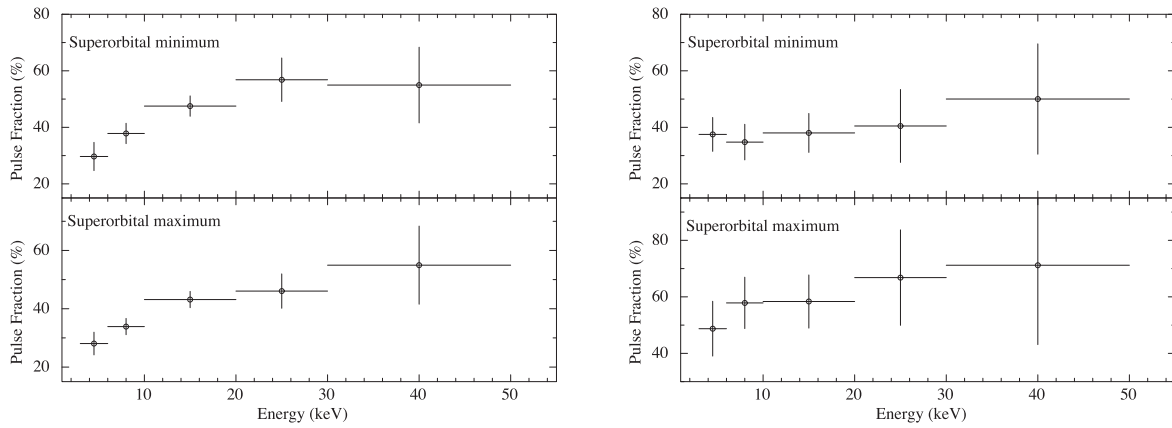


Figure 10. Energy dependence of the pulse fraction for 4U 1909 + 07 (left panel) and IGR J16418–4532 (right panel) for the NuSTAR observations at the predicted superorbital minimum and maximum phases.

predicted superorbital minimum and maximum observations of 4U 1909 + 07 are shown in the left panel of Figure 14. For the pulse-phase-resolved spectral study of IGR J16418–4532, we use a `HIGHECUT` modified by an absorption component to model the pulse-phase-resolved spectra. The cutoff energy E_C and the fold energy E_F were fixed to its phase-average values mentioned in Table 3 because these spectral parameters cannot be independently constrained during the spectral fits due to low statistics of the pulse-phase-resolved spectra. The results of the pulse-phase-resolved spectral study for the predicted superorbital minimum and maximum observations of IGR J16418–4532 are shown in the right panel of Figure 14. The results of pulse-phase-resolved spectral analysis for 4U 1909 + 07 and IGR J16418–4532 (keeping the `HighECut` parameter fixed to its phase-averaged value for IGR J16418–4532) using a `CUTOFFPL` model modified by an absorption component exhibits a similar variation in its spectral parameters.

2.4. Pulse Period and Fractional RMS Amplitude Evolution

Figure 15 shows the long-term pulse period evolution of 4U 1909 + 07 and IGR J16418–4532, along with the fractional RMS) amplitude. The fractional RMS amplitude on the superorbital period and its uncertainty were calculated using 16.7 yr Swift BAT light curves with 750 day intervals and 1000 day intervals for 4U 1909 + 07 and IGR J16418–4532, respectively, with 50 day increments in the start and end times and using the fractional RMS formulation in Vaughan et al. (2003). The long-term pulse period evolution of 4U 1909 + 07 is shown in the left panel of Figure 15(a), using measurements from RXTE (Levine et al. 2004), INTEGRAL (Fürst et al. 2011), Suzaku (Fürst et al. 2012; Jaisawal et al. 2013), NuSTAR, and AstroSat (Jaisawal et al. 2020), along with the current NuSTAR measurements. The right panel of Figure 15(a) shows the pulse period evolution of IGR J16418–4532 from all previously reported XMM observations (Sidoli et al. 2012; Drave et al. 2013b). We do not use the spin-period value from Walter et al. (2006) due to the large error bars of 100 s on the measured value of the spin period. As mentioned in Section 2.2.2, we also estimate the pulse period from a previous 2015 NuSTAR observation and a 2019 XMM PN observation of the source to investigate the long-term spin-period evolution.

3. Discussion

3.1. Results from the Swift BAT Light Curves

From the dynamic power spectra constructed using the BAT light curves in the left panels of Figures 3(a), 4(a), and 5(a) for 4U 1909 + 07, IGR J16418–4532, and IGR J16479–4514, respectively, we see two prominent peaks at the fundamental superorbital period and the second harmonic, which strengthen and weaken approximately on the timescales of years. The presence of two peaks, one at the fundamental frequency of the superorbital period and the other at the second harmonic, was seen in the dynamic power spectrum of 4U 1538–52 (Corbet et al. 2021), although only a prominent peak at the superorbital period was seen in the dynamic power spectra of 2S 0114 + 650 (Hu et al. 2017) and IGR J16493–4348 (Coley et al. 2019).

We folded the different segments of the BAT light curve with the superorbital periods of the three sources to illustrate the changes in the shape of the superorbital intensity profiles on the different timescales of the modulations in the dynamic power spectra. Sections 2.1.2, 2.1.2, and 2.1.3 describe the different segments of the BAT light curves of 4U 1909 + 07, IGR J16418–4532, and IGR J16479–4514, respectively, where either the peak at the fundamental frequency or the second harmonic became stronger or weaker and consistent with the mean power. The right panels of Figures 3, 4, and 5 show the superorbital intensity profiles of 4U 1909 + 07, IGR J16418–4532, and IGR J16479–4514, respectively, at these different time segments. We calculated the fractional RMS f_{RMS} for the superorbital intensity profiles and found that the f_{RMS} is lower for the time periods where both the fundamental and harmonic modulations were not strongly present in the dynamic power spectrum.

Figure 15 shows the long-term pulse period evolution of 4U 1909 + 07 and IGR J16418–4532 using all available spin-period measurements from pointed observations (including the current work) and the RMS amplitude on the superorbital period constructed from the long-term Swift BAT light curves. The pulse period of the NS in 4U 1909 + 07 spun up from 604.8 to 602.9 s over ~ 18 yr, with an average spin-up rate of $4.7 \times 10^{-9} \text{ s s}^{-1}$. However, we see different trends of pulse period evolution and the fractional RMS amplitude for 4U 1909 + 07 on different timescales, which could be related to the changes in strengths of the superorbital modulation at the fundamental frequency and the second harmonic. For 4U

Table 4
Best-fitting Parameter Values for the Swift XRT + NuSTAR Spectra of IGR J16418–4532 Using the Models Defined in Section 2.3 for the Observations at the Predicted Superorbital Minimum and Maximum Phases, and a 2015 Observation

Parameters	HIGHECUT			CUTOFFPL			NPEX			FDCUT		
	Min	Max	2015	Min	Max	2015	Min	Max	2015	Min	Max	2015
C_{XRT}	0.93 ± 0.08	0.9 ± 0.1	...	0.87 ± 0.08	0.9 ± 0.1	...	0.89 ± 0.08	0.9 ± 0.1	...	0.93 ± 0.08	0.9 ± 0.1	...
C_{FPMB}	1.01 ± 0.01	1.03 ± 0.02	1.03 ± 0.01	1.01 ± 0.1	1.03 ± 0.02	1.03 ± 0.01	1.01 ± 0.01	1.03 ± 0.02	1.03 ± 0.01	1.01 ± 0.01	1.03 ± 0.02	1.02 ± 0.01
N_H^a	5.8 ± 0.5	7.1 ± 0.8	6.7 ± 0.4	3.3 ± 0.4	5 ± 1	5.5 ± 0.5	3.7 ± 0.4	5 ± 1	5.5 ± 0.5	5.6 ± 0.5	6.9 ± 0.8	6.3 ± 0.4
Γ	1.48 ± 0.02	1.66 ± 0.04	1.39 ± 0.02	1.0 ± 0.02	1.2 ± 0.1	1.18 ± 0.05	1.07 ± 0.02	1.2 ± 0.1	1.18 ± 0.05	1.46 ± 0.03	1.65 ± 0.05	1.35 ± 0.02
Norm ^b	8.8 ± 0.6	6.5 ± 0.6	10.3 ± 0.5	4.4 ± 0.2	3.4 ± 0.6	7.5 ± 0.6	4.8 ± 0.3	3.4 ± 0.6	7.5 ± 0.7	8.3 ± 0.6	6.3 ± 0.7	9.5 ± 0.5
Cutoff energy E_C^c	26^{+2}_{-2}	32 ± 3	24 ± 1	36.6 ± 0.8	40 ± 2	35.7 ± 0.6	...
Fold energy E_F^c	40^{+17}_{-12}	10 ± 4	30^{+6}_{-4}	30(fixed)	27^{+6}_{-5}	57^{+13}_{-9}	30(fixed)	27 ± 5	59^{+14}_{-9}	5.0 ± 0.7	4 ± 2	5.2 ± 0.5
gabs (LineE) ^c	53^{+24}_{-4}	...	59^{+46}_{-5}	53^{+6}_{-3}	...	56^{+5}_{-3}	52^{+6}_{-2}	...	56^{+5}_{-3}
gabs (σ) ^c	8^{+7}_{-2}	...	10^{+10}_{-2}	8^{+2}_{-1}	...	10^{+2}_{-1}	8 ± 2	...	10^{+2}_{-1}
gabs (Strength)	33^{+79}_{-13}	...	77^{+30}_{-29}	44^{+51}_{-12}	...	81^{+53}_{-20}	41^{+41}_{-11}	...	80^{+52}_{-21}
Fe $K\alpha^c$	6.3 ± 0.1	6.4(fixed)	6.3 ± 0.1	6.2 ± 0.1	6.4(fixed)	6.3 ± 0.1	6.3 ± 0.1	6.4(fixed)	6.2 ± 0.1	6.3 ± 0.1	6.4(fixed)	6.3 ± 0.1
Fe $K\alpha$ Norm ^d	2 ± 1	<0.3	4 ± 1	3 ± 1	<0.6	5 ± 1	3 ± 1	<0.6	5 ± 1	3 ± 1	<0.3	4 ± 1
Fe $K\alpha$ EW ^e	41 ± 21	<14	49 ± 15	69 ± 21	<28	57 ± 14	61 ± 20	<28	57 ± 15	45 ± 21	<14	51 ± 14
χ^2_ν/dof	1.00/252	0.98/249	0.89/240	1.15/254	1.12/250	0.94/240	1.15/254	1.12/256	0.96/239	1.03/252	0.98/249	0.84/240
Flux _s ^f	2.64 ± 0.03	1.35 ± 0.03	...	2.71 ± 0.04	1.37 ± 0.02	...	2.71 ± 0.02	1.37 ± 0.02	...	2.67 ± 0.03	1.35 ± 0.02	...
Flux _h ^g	11.9 ± 0.1	5.6 ± 0.2	17.3 ± 0.1	11.8 ± 0.1	5.8 ± 0.1	17.3 ± 0.1	11.7 ± 0.1	5.8 ± 0.1	17.2 ± 0.1	11.8 ± 0.1	5.6 ± 0.1	17.3 ± 0.1

Notes. The errors on the parameters are estimated using 90% confidence limits.

^a in units of 10^{22} cm^{-2} .

^b in units of $10^{-3} \text{ photons keV}^{-1} \text{ cm}^2 \text{ s}^{-1}$ at 1 keV.

^c in units of keV

^d in units of $10^{-5} \text{ photons cm}^2 \text{ s}^{-1}$.

^e EW is the equivalent width in units of eV.

^f unabsorbed X-ray flux in 0.5–8.0 keV in $10^{-11} \text{ erg s}^{-1} \text{ cm}^{-2}$.

^g unabsorbed X-ray flux in 3–60 keV in $10^{-11} \text{ erg s}^{-1} \text{ cm}^{-2}$.

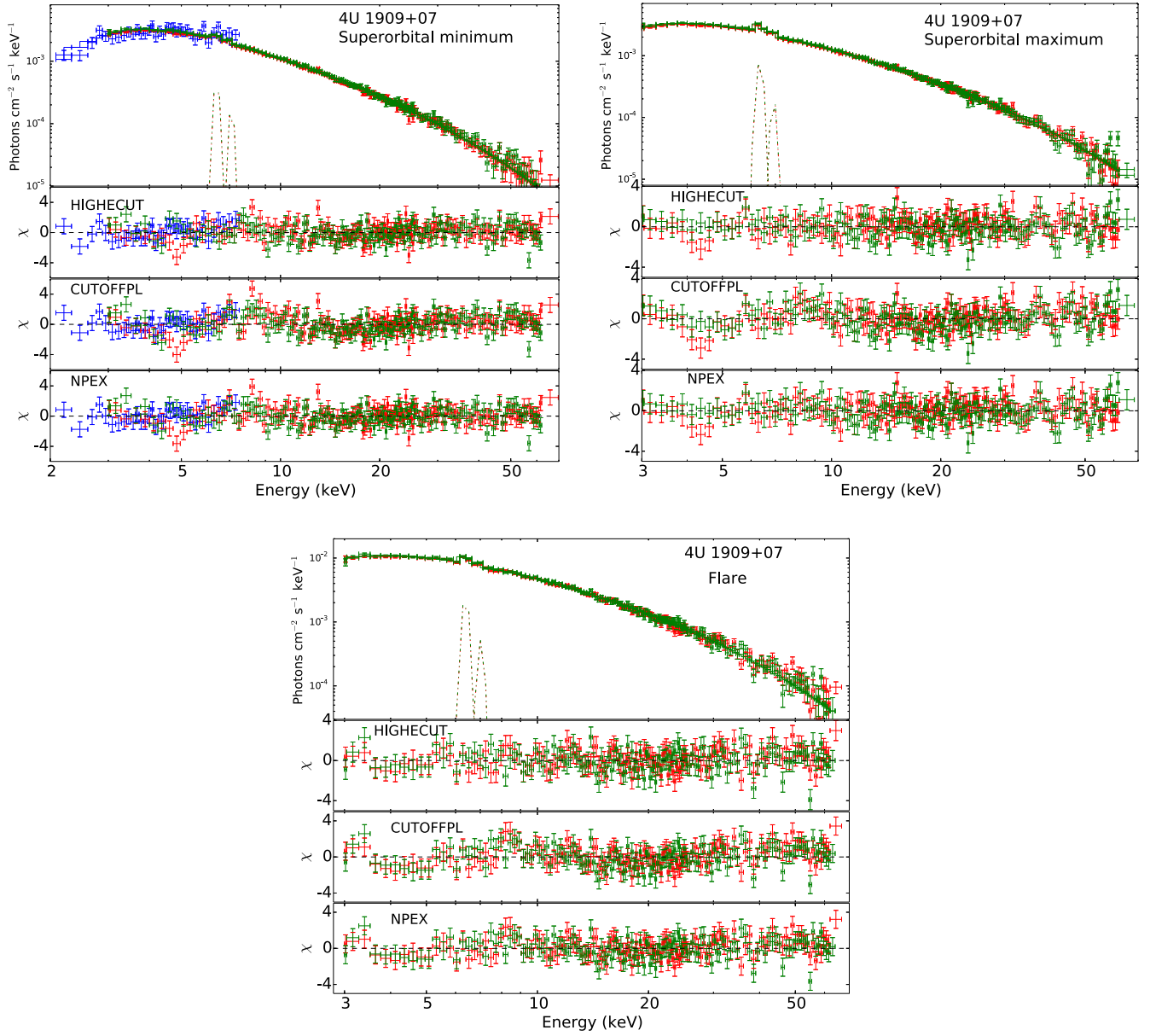


Figure 11. Pulse-phase-averaged spectra of 4U 1909 + 07 at the predicted superorbital minimum (left panel), maximum (right panel), and the X-ray flare (bottom panel). The top panel shows the spectra with Swift XRT (blue), NuSTAR FPMA (red), and FPMB (green). The bottom panels are the residuals to the fit using HIGHECUT, CUTOFFPL, and NPEX models. The spectra are rebinned for clarity

1538–52 and 2S 0114 + 650, two sgHMXBs showing super-orbital modulation, the strength of the superorbital modulation in the dynamic power spectra constructed with Swift BAT and RXTE ASM light curves, are apparently correlated with the spin-period changes \dot{P}_{spin} in the source (Hu et al. 2017; Corbet et al. 2021). For IGR J16493–4348, the decrease in the fractional RMS amplitude was found to be consistent with the weakening of the fundamental frequency of the superorbital modulation seen in the dynamic power spectrum (Coley et al. 2019).

For 4U 1909 + 07, a spin-up trend was observed until MJD 54,000, with an average spin-up rate $\dot{P} = (1.2 \pm 0.2) \times 10^{-8} \text{ s s}^{-1}$. The errors on the spin-period changes were estimated at 1σ confidence. From MJD 54,000 to 56,000, the spin period was steady around $\sim 604 \text{ s}$ with no significant spin-up or spin-down trend. The fractional RMS on the superorbital period of 4U 1909 + 07 (left panel of Figure 15(b)) have

similar amplitudes from MJD 54,000 to MJD 56,000. After MJD 57,000, the spin-up trend continued, with an average spin-up rate $\dot{P} = (9 \pm 1) \times 10^{-9} \text{ s s}^{-1}$. The fractional RMS on the superorbital period of 4U 1909 + 07 (left panel of Figure 15(b)) shows a decrease in the amplitude by 60% from the peak value around MJD 56,000 to MJD 57,000. From the dynamic power spectrum constructed for 4U 1909 + 07 in the left panel of Figure 3(a), the superorbital modulation around the fundamental period became weaker around MJD 55,000 and reappeared around MJD 57,000. This suggests a correlation between the spin-down trend, fractional RMS amplitude, and strength of the superorbital modulations for 4U 1909 + 07, similar to that seen for 4U 1538–52 and 2S 0114 + 650. However, the data on the spin-period evolution is sparse from MJD 56,000 to MJD 57,000, hence it is difficult to pinpoint the epoch at which the current spin-up trend started.

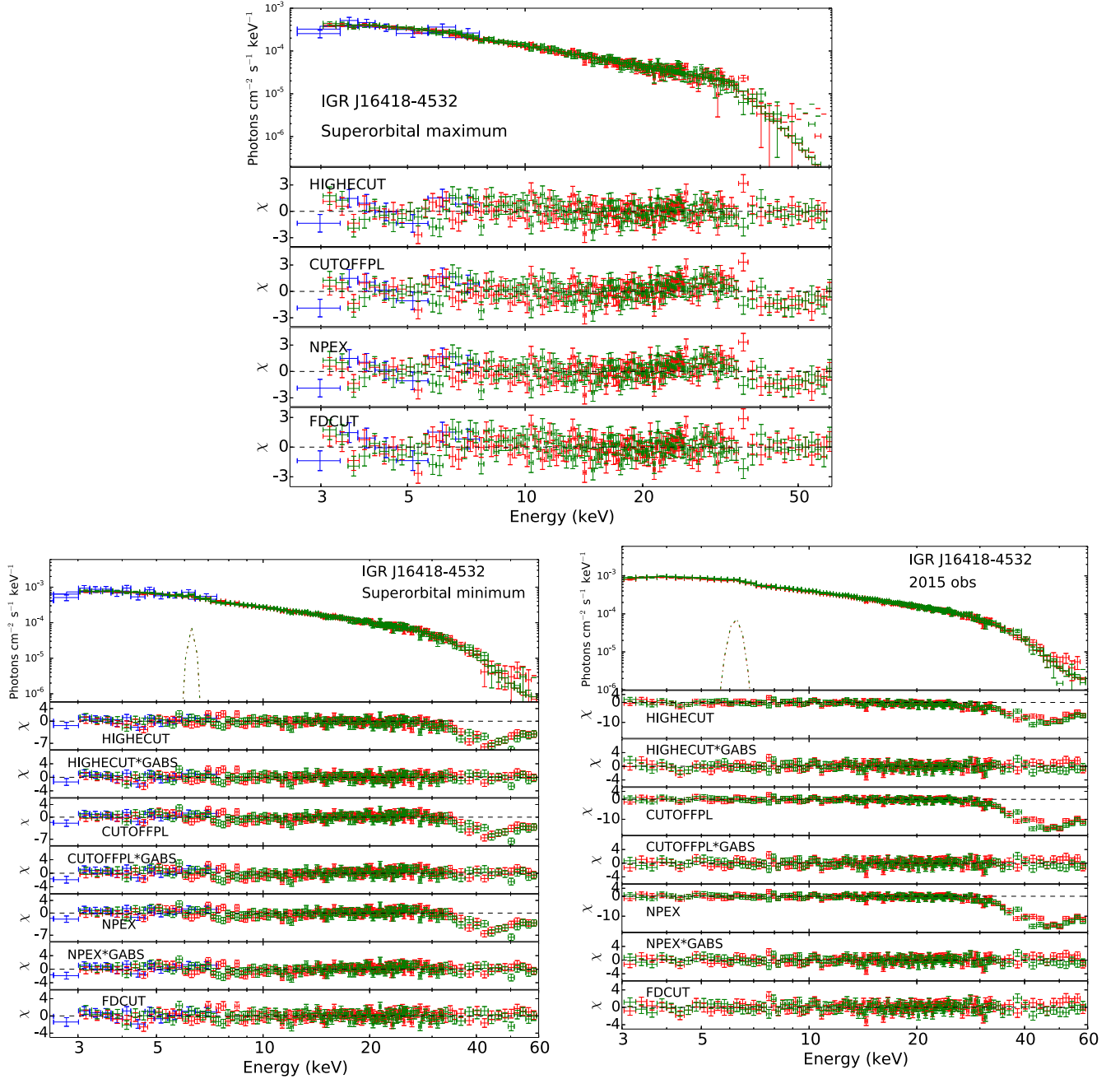


Figure 12. Pulse-phase-averaged spectra of IGR J16418–4532 at the predicted superorbital maximum (top panel) minimum (bottom left panel), and during the 2015 NuSTAR observation (bottom right panel); Swift XRT (blue), NuSTAR FPMA (red), and FPMB (green). The bottom panels are the residuals to the fit using HIGHECUT, CUTOFFPL, NPEX, and FDCUT models. We find absorption-like negative features ~ 50 keV in the residuals to the fit to HIGHECUT, CUTOFFPL, and NPEX for the superorbital minimum observation and the 2015 observation (bottom panel), which is fit with a absorption line with a Gaussian optical depth profile gabs. The spectra are rebinned for clarity.

The average spin-up rate of the pulsar in IGR J16418–4532 is $\dot{P} = (8 \pm 1) \times 10^{-9} \text{ s s}^{-1}$. The fractional RMS amplitude on the superorbital period of IGR J16418–4532 (right panel of Figure 15(b)) shows a decrease in the amplitude by 80% from its peak value around MJD 56,500 to MJD 58,000. From the dynamic power spectrum constructed for IGR J16418–4532 in the left panel of Figure 4(a), the superorbital modulation around the fundamental period became weaker around MJD 56,500 and reappears around MJD 58,000. This suggests a possible correlation between the strength of the fundamental period of the superorbital modulations and the fractional RMS amplitude. The pulse period histories of 4U 1909 + 07 and IGR

J16418–4532 are constructed using sparse pointed observations, unlike 4U 1538–52 and 2S 0114 + 650, which have been continuously monitored by Fermi GBM, RXTE ASM, and Swift BAT. Hence, it is difficult to correlate the changes in the pulse periods with their changes in the strengths of the superorbital modulation due to the lack of regular monitoring.

3.2. Results from the Swift XRT and NuSTAR Observations

3.2.1. Light Curves and Energy-resolved Pulse Profiles

The simultaneous Swift XRT and NuSTAR observations of the three sources were carried out at their predicted superorbital

Table 5

Best-fitting Parameter Values for the Swift XRT + NuSTAR Spectra of IGR J16479–4514, Excluding the Large X-ray Flares and Using the Models Defined in Section 2.3 for the Observations at the Predicted Superorbital Minimum and Maximum Phases

Parameters	HIGHECUT		CUTOFFPL		NPEX	
	Min	Max	Min	Max	Min	Max
C_{XRT}	...	1.8 ± 0.1	...	1.8 ± 0.1	...	1.8 ± 0.1
C_{FPMB}	0.99 ± 0.02	1.01 ± 0.02	0.99 ± 0.02	1.01 ± 0.02	0.99 ± 0.02	1.01 ± 0.02
N_{H}^{a}	7 ± 1	6 ± 1	8.1 ± 0.9	6.8 ± 0.9	8.1 ± 0.9	6.8 ± 0.9
Γ	1.3 ± 0.1	1.4 ± 0.1	1.28 ± 0.09	1.4 ± 0.1	0.77 ± 0.06	1.4 ± 0.1
Norm ^b	5 ± 1	6 ± 1	6 ± 1	7 ± 1	6 ± 1	7 ± 0.1
Cutoff energy E_{C}^{c}	$6.5^{+1.3}_{-0.8}$	6 ± 1
Fold energy E_{F}^{c}	29^{+9}_{-5}	32^{+10}_{-6}	27^{+6}_{-4}	26^{+7}_{-5}	27^{+6}_{-4}	27^{+7}_{-5}
χ^2_{ν}/dof	0.95/222	1.14/234	0.96/223	1.15/235	0.97/222	1.16/234
Flux _s ^d	...	4.39 ± 0.03	...	4.40 ± 0.02	...	4.39 ± 0.02
Flux _h ^e	6.9 ± 0.1	6.8 ± 0.1	6.9 ± 0.2	6.7 ± 0.1	6.9 ± 0.1	6.7 ± 0.1

Notes. The errors on the parameters are estimated using 90% confidence limits.

^a in units of 10^{22} cm^{-2} .

^b in units of $10^{-3} \text{ photons keV}^{-1} \text{ cm}^2 \text{ s}^{-1}$ at 1 keV.

^c in units of keV

^d unabsorbed X-ray flux in 0.5–8.0 keV in $10^{-11} \text{ erg s}^{-1} \text{ cm}^{-2}$.

^e unabsorbed X-ray flux in 3–40 keV in $10^{-11} \text{ erg s}^{-1} \text{ cm}^{-2}$.

maximum and minimum phases for a single superorbital cycle using the ephemerides given in Corbet & Krimm (2013). Unfortunately, these Swift XRT and NuSTAR observations were carried out when the peak of the fundamental frequencies of the superorbital modulations had weakened, as seen in the dynamic spectra of three sources in the left panels of Figures 3(a), 4(a), and 5(a).

The light curves and the hardness ratios of the NuSTAR observations of 4U 1909 + 07 are shown in Figure 6. There is a short X-ray flare, about ~ 3.3 ks in the NuSTAR observation, at the predicted superorbital maximum phase of 4U 1909 + 07. The hardness ratios remain constant throughout the observations. The energy-resolved pulse profiles in the left panel of Figure 9 exhibit a complex profile with a double-peaked structure and a dip profile at lower energies, evolving to a single-peak profile at higher energies. However, the shape of the energy-resolved pulse profiles in both observations is similar.

The NuSTAR light curve of IGR J16418–4532 in Figure 7 exhibits short X-ray flares lasting a few kiloseconds. The hardness ratios indicates a softening of the spectra during these short X-ray flares, which suggests accretion from a clumpy stellar wind around the SFXT. The energy-resolved pulse profiles shown in the right panel of Figure 9 are complex, with the predicted superorbital maximum and minimum observations having significant changes in the pulse profiles at lower energies. The complex behavior of pulse profiles at lower energies is usually indicative of a changing circumstellar environment around the NS, especially in the form of pulse-phase-locked matter (Kretschmar et al. 2019). Variations in the energy-resolved pulse phase profiles at different superorbital phases have been seen in Her X–1, which were attributed to the precessing accretion disks (Brumback et al. 2021). However, the superorbital modulation for IGR J16418–4532 was weaker at the time when the NuSTAR observations were carried out. So it is unlikely that the changes in the pulse profiles are related directly to the mechanism causing the superorbital modulation.

The NuSTAR light curves of IGR J16479–451 in Figure 8 show two large X-ray flares lasting a few kiloseconds, in addition to short X-ray flares lasting a few 100 s. Such large

X-ray flares in IGR J16479–4514 have been seen previously in Suzaku and INTEGRAL observations and are thought to be associated with the orbital phase-locked matter in the stellar wind of the supergiant star, in addition to the clumpy stellar wind of the SFXT system (Sidoli et al. 2012; Sguera et al. 2020). There is a softening of the hardness ratios during the large X-ray flares that suggests an increased mass accretion onto the compact object during these X-ray flares. We do not detect any pulsations from the NuSTAR light curves and provide an upper limit on the pulse fraction of 16% for a pulse period of 500–1000 s, the tentative spin-period range estimated from its expected position in the P_{spin} versus P_{orbital} diagram (Corbet 1986).

3.2.2. Pulse-phase-averaged and Pulse-phase-resolved Spectral Analysis

We jointly fit the NuSTAR spectra with the Swift XRT spectra where applicable, with four empirical spectral models: HIGHECUT, CUTOFFPL, NPEX, and FDCUT, modified with an absorption component to account for the circumstellar matter surrounding the NS and Gaussian lines for the Fe fluorescence emission lines where present. The results from the four empirical spectral models are used to check the consistency of the results.

The spectra of 4U 1909 + 07 with two NuSTAR observations along with one simultaneous Swift XRT observation were modeled using three empirical models: HIGHECUT, CUTOFFPL, and NPEX. We separately carried out the spectral fitting of the short X-ray flare in the light curve of the NuSTAR observation of the superorbital maximum. The spectrum of 4U 1909 + 07 shows strong Fe fluorescence lines: at 6.4 keV Fe $K\alpha$ with an equivalent width of ~ 70 eV, and at the 7.1 keV Fe $K\beta$ line with an equivalent width of ~ 30 eV. These strong Fe fluorescence lines have also been previously seen in a Suzaku (Fürst et al. 2012), NuSTAR, and AstroSat spectrum (Jaisawal et al. 2020) and are attributed to the dense circumstellar medium around the source $N_{\text{H}} \sim 7 \times 10^{22} \text{ cm}^{-2}$. Analysis of a previous Suzaku observation by Jaisawal et al. (2013) detected a CRSF at ~ 44 keV. However, we do not find any negative

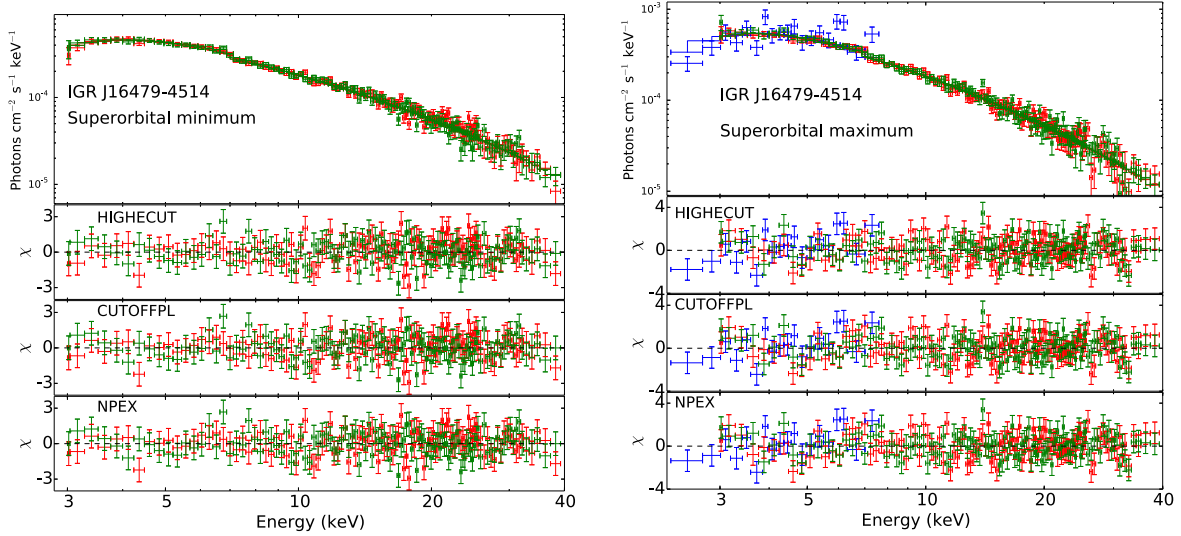


Figure 13. Pulse-phase-averaged spectra of IGR J16479–4514 at the predicted superorbital minimum (left panel) and maximum (right panel), excluding the large X-ray flares. The top panel shows the spectra with Swift XRT (blue), NuSTAR FPMA (red), and FPMB (green). The bottom panels are the residuals to the fit using the HIGHECUT, CUTOFFPL, and NPEX models. The spectra are rebinned for clarity.

residuals in the spectra from either observation, which is consistent with the null detection of any such negative residuals in the previous NuSTAR spectra by Jaisawal et al. (2020). The values of the spectral parameters absorption column density N_{H} , photon index Γ , cutoff energy E_{C} , folding energy E_{F} , and the X-ray fluxes are similar for the superorbital minimum and maximum observations. For the spectra of the short X-ray flare, the absorption column density N_{H} remains similar; the photon index Γ becomes harder, however, with an increase in the X-ray flux. For a distance of 4.85 kpc, the X-ray luminosity for the observations without the X-ray flare in the energy band of 3–70 keV was $\sim 1.3 \times 10^{36} \text{ erg s}^{-1}$ and that for the X-ray flare was $\sim 5 \times 10^{36} \text{ erg s}^{-1}$. This suggests an increase in mass accretion, leading to the X-ray flare, as seen for low to intermediate accretion rates in X-ray pulsars (Becker et al. 2012; Ballhausen et al. 2017).

The broadband Swift XRT and NuSTAR spectra of IGR J16418–4532 were fit with all four empirical spectral models: HIGHECUT, CUTOFFPL, NPEX, and FDCUT. The spectra from the predicted superorbital minimum observation and a previous 2015 NuSTAR show a 6.4 keV Fe $K\alpha$ line, which was modeled by a Gaussian line. This line has previously been seen in the spectrum from an XMM observation (Drave et al. 2013b). However, no strong residuals around the 6.4 keV Fe $K\alpha$ line were seen in the predicted superorbital maximum spectra, mostly likely due to the short observation time compared to the other two observations. We estimated the upper limits of the equivalent width and line flux of an Fe $K\alpha$ line for the spectra of the observation by modeling a Gaussian line with a line center fixed at 6.4 keV and fitting the spectra. The absorption column density N_{H} and photon index Γ are similar for both observations. The X-ray flux was higher for the observation at the predicted superorbital minimum phase than the predicted maximum phase, which is most likely due to the longer duration of the observation and hence the presence of more X-ray flares. For a distance of 13 kpc, the X-ray luminosity of the observation at the predicted superorbital maximum phase in the energy band of 3–60 keV was $\sim 1.2 \times 10^{36} \text{ erg s}^{-1}$ and that at the predicted superorbital minimum phase and the 2015 observation was $\sim 3 \times 10^{36} \text{ erg s}^{-1}$. The negative absorption-

like features in the residuals to the spectral fits of the predicted superorbital minimum observation and a previous 2015 observation in Figure 12 seen for the residuals in the spectral fits to HIGHECUT, CUTOFFPL, and NPEX models, were modeled by an absorption line with a Gaussian optical depth profile g_{abs} . The statistical significance of this absorption-like feature is low, as mentioned in Section 2.3.2, and hence we do not confirm or firmly rule out the presence of a CRSF in the spectra from these observations.

The nonflaring part of the NuSTAR observation of IGR J16479–4514 along with one Swift XRT observation were fit with three empirical spectral models: HIGHECUT, CUTOFFPL, and NPEX. The large X-ray flares seen in the NuSTAR light curves will be studied in detail in a separate paper. The spectral parameters N_{H} , photon index Γ , cutoff energy E_{C} , folding energy E_{F} , and the X-ray fluxes are similar for the predicted superorbital minimum and maximum phases, indicating no change in the spectral characteristics at the superorbital phases. For a distance of 4.5 kpc, the X-ray luminosity of the nonflaring part of the observation in the energy band of 3–40 keV was $\sim 2 \times 10^{35} \text{ erg s}^{-1}$, whereas in the large X-ray flares, the X-ray luminosities increased to $\sim 10^{37} \text{ erg s}^{-1}$.

The pulse-phase-resolved spectra of the NuSTAR observations of 4U 1909 + 07 in the energy range 3–50 keV were modeled with the spectral model HIGHECUT, modified with an absorption component and Gaussian lines to model the Fe $K\alpha$ and Fe $K\beta$ line. The spectral parameters of the Fe $K\beta$ line were kept fixed to the phase-averaged values. The left panel of Figure 14 shows the pulse-phase evolution of the spectral parameters of 4U 1909 + 07: absorption column density N_{H} , photon index Γ , cutoff energy E_{C} , folding energy E_{F} , and the unabsorbed X-ray fluxes (in 3–50 keV). The hardness ratios were estimated for light curves folded with the pulse period in 3–10 keV and 10–50 keV using Equation (1). The unabsorbed X-ray flux is higher for the predicted superorbital maximum observation due to the inclusion of the X-ray flare when carrying out pulse-phase-resolved spectral analysis. The hardness ratios indicate a harder spectrum around the primary peak at pulse phase 0, and a softer spectrum around the secondary broader peak at pulse phase 0.5. We see a variation in the

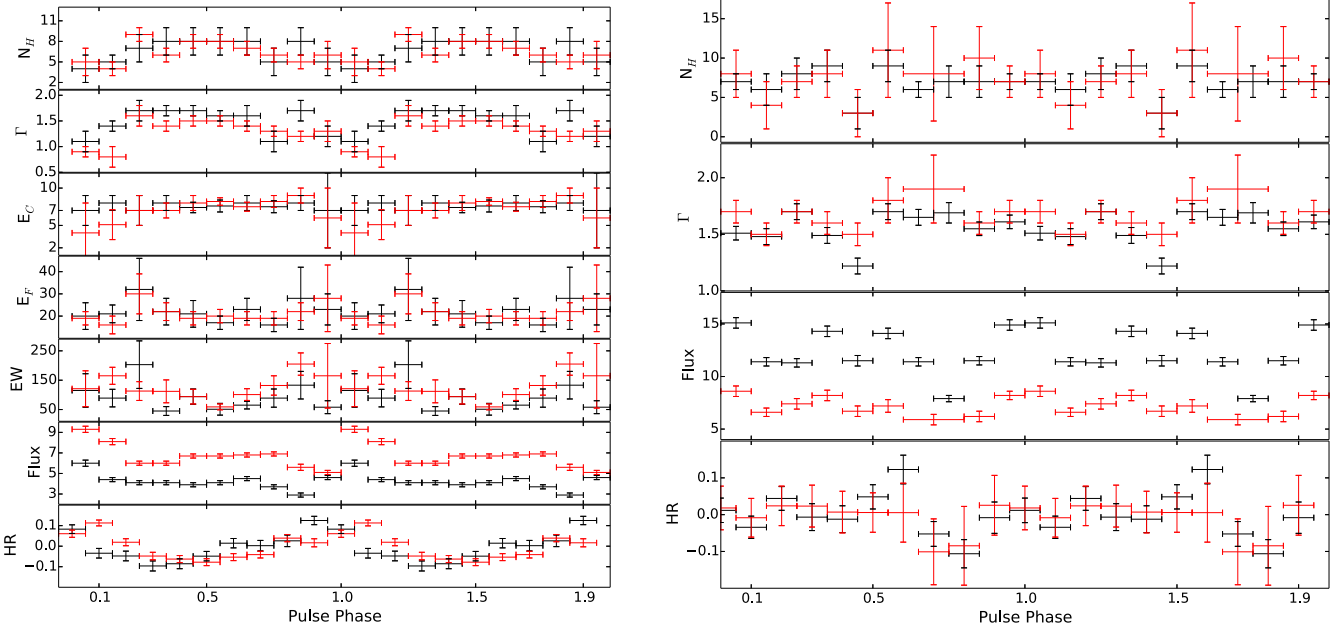


Figure 14. Left panel: pulse-phase-resolved spectra of 4U 1909 + 07 at the predicted superorbital minimum (black data points) and maximum (red data points) with a *HIGHECUT* model, modified by an absorption component. Right panel: pulse-phase-resolved spectra of IGR J16418–4532 at the predicted superorbital minimum (black data points) and maximum (red data points) with a *HIGHECUT* model, modified by an absorption component. The cutoff energy E_C and the folding energy E_F were fixed to its phase-average values. Units of N_H are in 10^{22} cm^{-2} , E_C in keV, E_F in keV, the equivalent width of an Fe $K\alpha$ line (EW) is in eV, and the unabsorbed X-ray flux (3–50 keV) is in units of $10^{-10} \text{ erg cm}^{-2} \text{ s}^{-1}$. The errors on the parameters are estimated using 90% confidence limits. The hardness ratios were estimated for light curves folded with the pulse period in 3–10 keV and 10–50 keV energy bands using Equation (1).

absorption column density N_H , photon index Γ , and the equivalent width of an Fe $K\alpha$ line as a function of the pulse phase, similar to the results of pulse-phase-resolved spectroscopic studies using a previous Suzaku observation by Fürst et al. (2012) and the NuSTAR observation by Jaisawal et al. (2020). A harder photon index $\Gamma \sim 1$ is seen at the pulse phase 0–0.2 for a lower value of $N_H \sim 5 \times 10^{22} \text{ cm}^{-2}$ at higher unabsorbed X-ray fluxes, which suggests higher accretion rates at these pulse phases. However, the spectral evolution as a function of the pulse phase remains similar for both observations, indicating no change in the emission properties at the predicted superorbital maximum and minimum phase.

For IGR J16418–4532, the energy-resolved pulse profiles exhibit a complex morphology at lower energies (left panel of Figure 9) that are uncorrelated to its superorbital phase. These structures in the pulse profiles at lower energies are most likely related to a variation of the absorption column densities and/or photon index Γ as a function of the pulse phase. The pulse-phase-resolved NuSTAR spectra of IGR J16418–4532 in the energy range 3–50 keV were modeled with a *HIGHECUT* model with the cutoff energy E_C , and the fold energy E_F was fixed to its phase-average values. The right panel of Figure 14 shows the pulse-phase evolution of the spectral parameters absorption column density N_H , photon index Γ and unabsorbed X-ray flux (in 3–50 keV). The hardness ratios were estimated for light curves folded with the pulse period in the energy bands 3–10 and 10–50 keV using Equation (1). As seen in the phase-averaged spectral analysis, the X-ray flux during the predicted superorbital minimum observation is higher than that during the predicted superorbital maximum observation. The hardness ratios indicate a spectral softening around pulse phase 0.7–0.9, which corresponds to the trough in the pulse profiles. However, due to limited statistics of the pulse-phase-resolved spectra, we cannot infer any strong variations in the absorption

column density N_H and photon index Γ as a function of a pulse phase. The spectral evolution as a function of pulse phase remains similar for both observations, indicating no change in the emission properties at the predicted superorbital maximum and minimum phases.

3.3. Comparison with Different Models of Superorbital Modulations

3.3.1. Precession of Accretion Disks

The superorbital modulations seen in Her X–1, SMC X–1, and LMC X–4 have been attributed to the precession of the warped and tilted accretion disk, which also leads to changes in the superorbital periods; for example, the superorbital modulation in SMC X–1 varies from 39 to 72 days (Ogilvie & Dubus 2001; Clarkson et al. 2003). The quasi-stable nature of the superorbital modulation seen in the dynamic power spectra with long-term Swift BAT light curves for 4U 1909 + 07, IGR J16418–4532, and IGR J16479–4514 (seen in left panels of Figures 3(a), 4(a), and 5(a)) suggests the absence of stable accretion disks in the system. Transient accretion disks have been observed in a few sgHMXBs such as OAO 1657–415 (Jenke et al. 2012) and 2S 0114 + 650 (Hu et al. 2017). In these systems, the NS is expected to spin up when a transient accretion disk is present. The spin-period evolution seen in 2S 0114 + 650 is found to be correlated with the strength of its superorbital modulations and is anticorrelated with the X-ray fluxes, most likely indicating a transition from a direct stellar wind to disk-stellar wind accretion (Hu et al. 2017). The transient accretion disk lasting for 1000–1500 days could also explain the weakening or strengthening of the superorbital modulations in 2S 0114 + 650, although the mechanism triggering the formation of such a transient accretion disk is unclear.

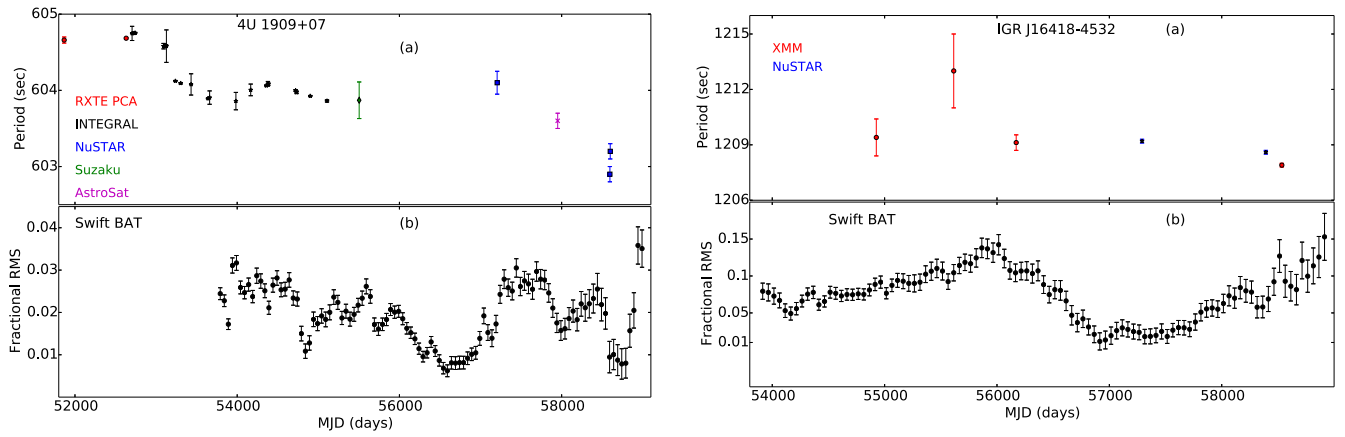


Figure 15. Left panel: long-term spin-period evolution of 4U 1909 + 07 (a) and the fractional RMS amplitude (b) calculated using a Swift BAT light curve with 750 day intervals, with 50 day increments in the start and end times. The measurement of spin periods of 4U 1909 + 07 are from previously reported values using RXTE PCA (Levine et al. 2004), INTEGRAL (Fürst et al. 2011), Suzaku (Fürst et al. 2012; Jaisawal et al. 2013), NuSTAR, and AstroSat observations (Jaisawal et al. 2020) as well from the current work. Right panel: long-term spin-period evolution of IGR J16418–4532 (a) and the fractional RMS amplitude (b) calculated using a Swift BAT light curve with 1000 day intervals, with 50 day increments in the start and end times. The measurement of spin periods of IGR J16418–4532 are from XMM observations previously reported in the literature (Sidoli et al. 2012; Drave et al. 2013b) as well as the estimates from the current and a previous 2015 NuSTAR observations and a 2019 XMM observation.

However, there have been no indications of a transient accretion disk in any of the five other sgHMXB systems where superorbital modulation has been conclusively detected: 4U 1909 + 07, IGR J16418–4532, IGR J16479–4514, IGR J16493–4348, and 4U 1538–522. For 4U 1538–522, the torque reversals are found to be uncorrelated with the X-ray fluxes (Corbet et al. 2021). For many of these sgHMXBs showing superorbital modulation, there were times seen in their dynamic power spectra during which the second harmonic was stronger than the fundamental frequency of the superorbital period. The current model of the precessing accretion disks is unable to account for these changes.

3.3.2. Tidally Induced Oscillations

Tidal oscillations from a nonsynchronously rotating donor star can exhibit different periodicities of the superorbital modulations (Koenigsberger et al. 2006; Toledano et al. 2007). These oscillations could produce a localized structured stellar wind from the donor star that could lead to superorbital modulation seen when this stellar wind interacts with the NS and becomes accreted. Tidal oscillations are predicted for systems with circular orbits, which is the case for many of the sgHMXBs, except for 4U 1538–52, which might have an eccentric orbit (Clark 2000; Hemphill et al. 2019). However, the tidal circularization timescales for asynchronously rotating stars (Zahn 1977; Hut 1981; Toledano et al. 2007) fail to account for the quasi-stable nature of the superorbital modulations on timescale of years seen in the Swift BAT dynamic power spectra of 4U 1909 + 07, IGR J16418–4532, IGR J16479–4514 (left panels of Figures 3(a), 4(a), 5(a)), IGR J16493–4348 (Coley et al. 2019), and 4U 1538–52 (Corbet et al. 2021). Tidal oscillations can be present in sources with eccentric orbits; the model predicts that the modulation will be observed near the binary orbital period (Moreno et al. 2011).

3.3.3. Corotating Interaction Regions in the Supergiant Wind

A large-scale CIR formed in the stellar wind of the supergiant stars can account for the observed superorbital

variability in sgHMXBs. The quasi-stable nature of the modulations and the changing shapes of the superorbital intensity profiles provide a stronger justification for the CIR model as the mechanism driving these superorbital modulations in sgHMXBs. The clumpy stellar winds in sgHMXBs are the main reason for the X-ray variabilities seen in sgHMXBs and its subclass SFXTs (Martínez-Núñez et al. 2017). The large structures in the stellar winds of OB supergiant stars in the form of discrete absorption components (DACs) has been confirmed using optical/UV spectroscopy (Underhill 1975; Howarth et al. 1984). These larger structures are thought to be formed due to irregularities on the stellar surface related either to dark/bright spots, magnetic loops, or nonradial pulsations causing spiral-shaped density and velocity perturbations in the stellar wind up to several tens of stellar radii. The interactions of these CIRs with the NS have been proposed to be the driving mechanisms for the superorbital modulations (Bozzo et al. 2017). The quasi-stable nature of the superorbital modulations seen in the sgHMXBs provides constraints on the formation and dissipation of the CIRs in the stellar winds of the OB supergiant stars.

Corbet et al. (2021) showed a tight correlation between the orbital period of a CIR with that of the orbital period of the sgHMXBs, indicating a pseudo-synchronization of the CIRs with the orbit of the NS. This pseudo-synchronization could be driven by the tidal synchronization or differential rotation of the primary star. A change in the superorbital modulation profile with the harmonic becoming stronger or weaker, as seen in the dynamic power spectra of 4U 1909 + 07, IGR J16418–4532, and IGR J16479–4514, suggests a change in the CIR structures in the stellar winds of these supergiant stars. One favorable scenario could be the appearance of multiple CIR structures in the supergiant stellar winds (Bozzo et al. 2017). As shown in Figure 3 of Bozzo et al. (2017), the NS in the sgHMXB system crossing two CIRs would produce a double-peaked superorbital modulation profile. A single CIR would explain only the fundamental frequency of superorbital modulations in 2S 0114 + 650 (Hu et al. 2017) and IGR J16493–4348 (Coley et al. 2019).

4. Summary

In this paper, we have investigated the superorbital modulations seen in the three sgHMXBs, 4U 1909 + 07, IGR J16418–4532, and IGR J16479–4514, using long-term Swift BAT light curves and pointed Swift XRT and NuSTAR observations. The Swift BAT light curves do not exhibit any significant long-term intensity variations between the different superorbital cycles for any of the three sources. The power spectra constructed from the Swift BAT light curves show the peak at the fundamental frequency and the second harmonic of the superorbital modulations for all the three sources. The strengths of the peaks at fundamental frequencies of the superorbital modulation and the second harmonics vary on typical timescales of years, as seen in their dynamic power spectra. The results suggest multiple CIRs in the stellar winds of the supergiant stars. However, structured wind due to tidal oscillations cannot be ruled out conclusively.

The pointed Swift XRT and NuSTAR observations for the three sources were scheduled to be carried out at the predicted superorbital maximum and minimum of the same superorbital cycle using the ephemerides given in Corbet & Krimm (2013). However, the observations occurred at the times when the superorbital modulation at the fundamental frequency was no longer strongly present for all the three sources. Hence, we do not find any significant changes between the spectral parameters of the predicted superorbital maximum and minimum phase. The NuSTAR spectra of 4U 1909 + 07 show a strong Fe K α line at ~ 6.4 keV and Fe K β line at ~ 7.1 keV. A 3 ks X-ray flare is seen in the light curve of 4U 1909 + 07, with an unabsorbed X-ray flux of $\sim 2 \times 10^{-9}$ erg cm $^{-2}$ s $^{-1}$. The spectral hardening during the X-ray flare without a change in the absorption column density N_H suggests an increase in mass accretion at low or intermediate accretion rates. The light curves of IGR J16418–4532 exhibit short X-ray flares, and the hardness ratios indicate spectral softening during the flares. The negative absorption-like residuals are seen in the spectral fits to the spectral models (except in the FDCUT model) for the predicted superorbital minimum observation and a previous 2015 observation could be an artifact of spectral modeling or a CRSF that could not be confirmed or ruled out in our analysis. The light curves of IGR J16479–4514 shows large X-ray flares that could be related to the orbital phase-locked X-ray flares present in this system. We do not find pulsations in the light curves and provide an upper limit of 16% on the pulse fraction for the putative NS in the pulse period range of 500–1000 s.

The energy-resolved pulse profiles of 4U 1909 + 07 and IGR J16418–4532 in Figure 9 exhibit a complex profile at energies ≤ 20 keV, which evolves to a single-peak profile at higher energies. However, these changes in the energy-resolved pulse profiles are unrelated to their superorbital modulations. The evolution of spectral parameters from pulse-phase-resolved spectroscopic studies of 4U 1909 + 07 and IGR J16418–4532 were similar for the predicted superorbital minimum and maximum observations. The pulse period evolution of 4U 1909 + 07 in the left panel of Figure 15(a) shows a possible correlation between the spin-period changes, fractional RMS amplitude, and changes in the strength of the superorbital modulations, similar to that seen for 2S 0114 + 650 and 4U 1538–52 (Hu et al. 2017; Corbet et al. 2021). Regular monitoring programs of 4U 1909 + 07 and IGR J16418–4532 with more sensitive all-sky monitors such as the enhanced X-ray Timing and Polarimetry mission (eXTP;

Zhang et al. 2016) or with pointed observatories such as NICER, NuSTAR, and AstroSat will be crucial for understanding the correlations between the spin-period changes, changes in the spectral parameters, and the strength of the superorbital modulations.

We thank the referee for insightful comments that have helped us improve the manuscript. The scientific results reported here are based on observations made by the NuSTAR X-ray observatory, and we thank the NuSTAR Operations, Software, and Calibration teams for scheduling and the execution of these observations. We have used the public light curves from the Swift BAT transient monitor provided by the Swift BAT team. Support for this work was provided by NASA through grant No. 80NSSC20K0036 and NASA award number 80GSFC21M0002. This research has made use of software provided by the XRT Data Analysis Software (XRTDAS) developed under the responsibility of the ASI Science Data Center (ASDC), Italy, and the NuSTAR Data Analysis Software (NuSTARDAS) jointly developed by the ASI Science Data Center (ASDC, Italy) and the California Institute of Technology. This research has made use of data and/or software provided by the High Energy Astrophysics Science Archive Research Center (HEASARC), which is a service of the Astrophysics Science Division at NASA/GSFC.

Software: XSPEC (v12.12.0; Arnaud 1996); ROBOT (Corbet et al. 1992).

ORCID iDs

Nazma Islam  <https://orcid.org/0000-0002-2413-9301>
 Robin H. D. Corbet  <https://orcid.org/0000-0002-3396-651X>
 Joel B. Coley  <https://orcid.org/0000-0001-7532-8359>
 Katja Pottschmidt  <https://orcid.org/0000-0002-4656-6881>
 Felix Fuerst  <https://orcid.org/0000-0003-0388-0560>

References

- Arnaud, K. A. 1996, in ASP Conf. Ser. 101, *Astronomical Data Analysis Software and Systems V*, ed. G. H. Jacoby & J. Barnes (San Francisco, CA: ASP), 17
- Asplund, M., Grevesse, N., Sauval, A. J., & Scott, P. 2009, *ARA&A*, 47, 481
- Ballhausen, R., Pottschmidt, K., Fürst, F., et al. 2017, *A&A*, 608, A105
- Barthelmy, S. D., Barbier, L. M., Cummings, J. R., et al. 2005, *SSRv*, 120, 143
- Becker, P. A., Klochkov, D., Schönherr, G., et al. 2012, *A&A*, 544, A123
- Bozzo, E., Giunta, A., Stella, L., et al. 2009, *A&A*, 502, 21
- Bozzo, E., Oskina, L., Lobel, A., & Hamann, W. R. 2017, *A&A*, 606, L10
- Brightman, M., Harrison, F. A., Bachetti, M., et al. 2019, *ApJ*, 873, 115
- Brumback, M. C., Hickox, R. C., Fürst, F. S., et al. 2020, *ApJ*, 888, 125
- Brumback, M. C., Hickox, R. C., Fürst, F. S., et al. 2021, *ApJ*, 909, 186
- Burrows, D. N., Hill, J. E., Nousek, J. A., et al. 2005, *SSRv*, 120, 165
- Chaty, S., Rahoui, F., Foellmi, C., et al. 2008, *A&A*, 484, 783
- Chou, Y., & Grindlay, J. E. 2001, *ApJ*, 563, 934
- Clark, G. W. 2000, *ApJL*, 542, L131
- Clarkson, W. I., Charles, P. A., Coe, M. J., et al. 2003, *MNRAS*, 339, 447
- Coleiro, A., Chaty, S., Zurita Heras, J. A., Rahoui, F., & Tomsick, J. A. 2013, *A&A*, 560, A108
- Coley, J. B., Corbet, R. H. D., Fürst, F., et al. 2019, *ApJ*, 879, 34
- Coley, J. B., Corbet, R. H. D., & Krimm, H. A. 2015, *ApJ*, 808, 140
- Corbet, R., Barbier, L., Barthelmy, S., et al. 2006, *ATel*, 779, 1
- Corbet, R., Markwardt, C., Barbier, L., et al. 2007, *PTPS*, 169, 200
- Corbet, R. H. D. 1986, *MNRAS*, 220, 1047
- Corbet, R. H. D., Coley, J. B., Krimm, H. A., Pottschmidt, K., & Roche, P. 2021, *ApJ*, 906, 13
- Corbet, R. H. D., & Krimm, H. A. 2013, *ApJ*, 778, 45
- Corbet, R. H. D., Larkin, C., & Nousek, J. A. 1992, in ASP Conf. Ser. 25, *Astronomical Data Analysis Software and Systems I*, ed. D. M. Worrall, C. Biemesderfer, & J. Barnes (San Francisco, CA: ASP), 106

- Corbet, R. H. D., Sokolowski, J. L., Mukai, K., Markwardt, C. B., & Tueller, J. 2008, *ApJ*, **675**, 1424
- Drave, S. P., Bird, A. J., Goossens, M. E., et al. 2013a, *ATel*, **5131**, 1
- Drave, S. P., Bird, A. J., Sidoli, L., et al. 2013b, *MNRAS*, **433**, 528
- Ducci, L., Sidoli, L., & Paizis, A. 2010, *MNRAS*, **408**, 1540
- Farrell, S. A., Sood, R. K., & O'Neill, P. M. 2006, *MNRAS*, **367**, 1457
- Farrell, S. A., Sood, R. K., O'Neill, P. M., & Dieters, S. 2008, *MNRAS*, **389**, 608
- Fürst, F., Kreykenbohm, I., Suchy, S., et al. 2011, *A&A*, **525**, A73
- Fürst, F., Pottschmidt, K., Kreykenbohm, I., et al. 2012, *A&A*, **547**, A2
- Harrison, F. A., Craig, W. W., Christensen, F. E., et al. 2013, *ApJ*, **770**, 103
- Hemphill, P. B., Rothschild, R. E., Cheatham, D. M., et al. 2019, *ApJ*, **873**, 62
- Horne, J. H., & Baliunas, S. L. 1986, *ApJ*, **302**, 757
- Howarth, I. D., Prinja, R. K., & Willis, A. J. 1984, *MNRAS*, **208**, 525
- Hu, C.-P., Chou, Y., Ng, C. Y., Lin, L. C.-C., & Yen, D. C.-C. 2017, *ApJ*, **844**, 16
- Hu, C.-P., Mihara, T., Sugizaki, M., Ueda, Y., & Enoto, T. 2019, *ApJ*, **885**, 123
- Hut, P. 1981, *A&A*, **99**, 126
- Jain, C., Paul, B., & Dutta, A. 2009, *MNRAS Lett.*, **397**, L11
- Jaisawal, G. K., Naik, S., Ho, W. C. G., et al. 2020, *MNRAS*, **498**, 4830
- Jaisawal, G. K., Naik, S., & Paul, B. 2013, *ApJ*, **779**, 54
- Jenke, P. A., Finger, M. H., Wilson-Hodge, C. A., & Camero-Arranz, A. 2012, *ApJ*, **759**, 124
- Koenigsberger, G., Georgiev, L., Moreno, E., et al. 2006, *A&A*, **458**, 513
- Kretschmar, P., Fürst, F., Sidoli, L., et al. 2019, *NewAR*, **86**, 101546
- Krimm, H. A., Holland, S. T., Corbet, R. H. D., et al. 2013, *ApJS*, **209**, 14
- Lang, F. L., Levine, A. M., Bautz, M., et al. 1981, *ApJL*, **246**, L21
- Leahy, D. A. 1987, *A&A*, **180**, 275
- Leahy, D. A. 2002, *MNRAS*, **334**, 847
- Levine, A. M., Rappaport, S., Remillard, R., & Savcheva, A. 2004, *ApJ*, **617**, 1284
- Martínez-Núñez, S., Kretschmar, P., Bozzo, E., et al. 2017, *SSRv*, **212**, 59
- Martínez-Núñez, S., Sander, A., Gímenez-García, A., et al. 2015, *A&A*, **578**, A107
- Mihara, T. 1995, PhD thesis, Univ. Tokyo, Japan
- Moreno, E., Koenigsberger, G., & Harrington, D. M. 2011, *A&A*, **528**, A48
- Ogilvie, G. I., & Dubus, G. 2001, *MNRAS*, **320**, 485
- Postnov, K., Shakura, N., Staubert, R., et al. 2013, *MNRAS*, **435**, 1147
- Protassov, R., van Dyk, D. A., Connors, A., Kashyap, V. L., & Siemiginowska, A. 2002, *ApJ*, **571**, 545
- Rajolimanana, A. F., Charles, P. A., & Udalski, A. 2011, *MNRAS*, **413**, 1600
- Romano, P., Barthelmy, S. D., Kennea, J. A., et al. 2012a, *ATel*, **4148**, 1
- Romano, P., Barthelmy, S. D., Krimm, H. A., et al. 2015, *ATel*, **7454**, 1
- Romano, P., Mangano, V., Ducci, L., et al. 2012b, *MNRAS*, **419**, 2695
- Romano, P., Sidoli, L., Mangano, V., et al. 2008, *ApJL*, **680**, L137
- Scargle, J. D. 1982, *ApJ*, **263**, 835
- Sguera, V., Bassani, L., Landi, R., et al. 2008, *A&A*, **487**, 619
- Sguera, V., Bazzano, A., Bird, A. J., et al. 2006, *ApJ*, **646**, 452
- Sguera, V., Tiengo, A., Sidoli, L., & Bird, A. J. 2020, *ApJ*, **900**, 22
- Sidoli, L., Esposito, P., Sguera, V., et al. 2013, *MNRAS*, **429**, 2763
- Sidoli, L., Mereghetti, S., Sguera, V., & Pizzolato, F. 2012, *MNRAS*, **420**, 554
- Staubert, R., Klochkov, D., Postnov, K., et al. 2009, *A&A*, **494**, 1025
- Tanaka, Y. 1986, in *Observations of Compact*, ed. D. Mihalas & K.-H. A. Winkler, Vol. 255 (Berlin: Springer), 198
- Toledano, O., Moreno, E., Koenigsberger, G., Detmers, R., & Langer, N. 2007, *A&A*, **461**, 1057
- Torrejón, J. M., Schulz, N. S., Nowak, M. A., & Kallman, T. R. 2010, *ApJ*, **715**, 947
- Townsend, L. J., & Charles, P. A. 2020, *MNRAS*, **495**, 139
- Underhill, A. B. 1975, *ApJ*, **199**, 691
- Vaughan, S. 2005, *A&A*, **431**, 391
- Vaughan, S., Edelson, R., Warwick, R. S., & Uttley, P. 2003, *MNRAS*, **345**, 1271
- Verner, D. A., Ferland, G. J., Korista, K. T., & Yakovlev, D. G. 1996, *ApJ*, **465**, 487
- Walter, R., Zurita Heras, J., Bassani, L., et al. 2006, *A&A*, **453**, 133
- Walton, D. J., Fürst, F., Bachetti, M., et al. 2016, *ApJL*, **827**, L13
- White, N. E., Swank, J. H., & Holt, S. S. 1983, *ApJ*, **270**, 711
- Wilms, J., Allen, A., & McCray, R. 2000, *ApJ*, **542**, 914
- Wojdowski, P., Clark, G. W., Levine, A. M., Woo, J. W., & Zhang, S. N. 1998, *ApJ*, **502**, 253
- Zahn, J. P. 1977, *A&A*, **500**, 121
- Zhang, S. N., Feroci, M., Santangelo, A., et al. 2016, *Proc. SPIE*, **9905**, 99051Q